Journal of Structural Dynamics, Special issue on Tribomechadynamics, (pp. 105-138) 2024
On comparing behavior and performance of underplatform dampers according to shape

On comparing behavior and performance of Underplatform Dampers according to shape

Muzio M. Gola*

Politecnico di Torino, Dept. Mechanical Aerospace Engineering, corso Duca degli Abruzzi 24, 10129, Torino, Italy

Abstract

This paper is the completion of a previous work in which an algorithm was developed for direct calculation of the hysteresis cycle of Underplatform Dampers (UDs) used for vibration damping of turbine blades.
While the previous paper examined the scalability of a given damper shape as a function of its size, platform size and contact parameters, this paper instead shows how the method can be used to evaluate the advantages and disadvantages of different damper shapes.
Only the asymmetric contact damper is studied, in its simplest version with three pad-located contacts, and its merits are discussed in comparison with the wedge or cottage-roof type dampers, whose crucial difficulties are pointed out.
A family of five dampers obtained by distortion of an isosceles damper of 60° vertex aperture is studied as an example of application of the method. A criterion is defined for positioning the single contact to avoid lifting when the coefficient of friction is maximum at μ=0.7, then performance is studied for two values in the range expected for normal operation, μ =0.5 and μ=0.3.
For each of the five dampers, the different problems that arise in calculating the hysteresis cycle at the onset of the total full-slip, called Base-Cycle, are examined, first on the damper in terms of the “force Base-Cycle,” otherwise known as the “equilibrium trace diagram,” then of the “moment Base-Cycle” on the platform.
The “moment Base-Cycle” is employed in the context of the Platform Centered Reduction (PCR) technique, and diagrams of the real and imaginary components of the complex moment-rotation stiffness of the platform representing the mutual damper-platform actions are defined.
Finally, the values of the energies dissipated on the contact pads of the dampers are determined, the sum of which is checked against the total energy dissipated by the moment of the contact forces acting on the platform, consistent with the Platform Centered Reduction.
The parameters and diagrams that characterize the shape of a damper, regardless of its subsequent coupling with a specific turbine blade, are useful tools for characterizing its performance with greater insight than can be obtained from the usual purely numerical approach.

Keywords: Turbine blade, Vibration damping, Underplatform damper, Base-Cycle, Platform Centered Reduction, Damper shape

Received on June 20, 2024, Accepted on October 10, 2024, Published on December 6, 2024

1 Introduction

Turbine blades are subjected to vibrations that cause high cycle fatigue and can trigger cracks in highly stressed areas, leading to failure. To minimize vibrations, devices known as Underplatform Dampers (UDs), are placed between platforms of adjacent turbine blades. They are positioned so that, during turbine operation, centrifugal forces draw their lateral inclined friction faces into contact with the complementary inclined faces of platforms. These, placed circumferentially on the blades between the airfoil and the neck, are intended to create a continuity wall that separates the flow path acting on the airfoils from the cooling flow path on the neck. Circumferential gaps between the platforms are sealed by the dampers themselves. Vibrations of the blades cause relative motion between the damper-platform contact surfaces under compressive load. The energy dissipated by the resulting frictional forces reduces the vibration amplitude.

* muzio.gola@polito.it

Paper [1] of 1988 states that over the decade before its publication date research on turbine blade friction dampers had resulted in new methods to optimize damper design, while before blade damper design was a more a matter of "experience and very simple mathematical models". Paper [2] can be considered seminal for a systematic engineering approach to UDs.

Complementary lines have then been followed by other groups. In the impossibility of reviewing the overwhelming amount of activity, a historical summary can be made by examining in a selection of papers [3-16], the topics covered, their lines of development and their references.

Papers [1, 2], as well as their synthesis [17], deal with a flat damper, acting on parallel adjacent platforms, of the BG (Blade-to-Ground) type; damping capabilities are investigated by comparing a numerical model of a blade-damper system with their experimental counterpart. For a range of damper compressive normal load (N) and blade excitation (E) levels the resonance frequency (f) is found with associated response (R) amplitude; the damper-blade system is characterized by representing either the R/E vs. N/E or the R/N vs. E/N curves (in both cases loci of response maxima), the last being the damper performance curve. The key to this curve is to determine the normal load N such that the resonant response in terms of a local stress is less than an allowable value (e.g. fatigue endurance stress) for as large an excitation as possible, a concept insightfully commented by [8] in a broader context of concurring damping techniques.

After that initial stage numerical and experimental procedures were extended to blade-to-blade, self-centering, wedge dampers, as they provided more design flexibility to meet operating conditions [4, 5]. These papers have in common:

- platforms and damper are treated as rigid bodies,
- blade and platform motion is harmonic,
- damper and platform surfaces remain in parallel and in contact at all times,
- relative contact kinematics is calculated,
- tangential contact stiffness is considered, not normal stiffness
- vibration inertia forces of the damper are negligible,
- contact resultant forces are considered, acting on fixed "nodes" representing the platforms,
- in-plane damper equilibrium is represented by two translational equilibrium equations
- equilibrium of damper to rotation is missing.

Paper [5] claims to add 3-dimensional platforms, 2-dimensional contact motions and microslip.

Although these works had the merit of pursuing the essential characteristics of the damper-platform interaction, in the light of subsequent experience it is now all too easy to observe that the lack of rotational equilibrium leads to difficulties both on the stick-slip transition criteria [4] and on the determination of contact forces [5].

In [6] a "contact asymmetric" damper is first introduced, with a cylindrical contact on one platform and a flat contact on the opposite platform. The wedge damper is reported to be unsuitable in practical applications (as opposed, of course, to idealized numerical simulations) because of the practical impossibility of accurately aligning it within the platforms and having complete, controllable contact between the flat surfaces. Resulting in unpredictable damper positions due to a multiplicity of possible edge contacts and likely cyclic impacts on the damper edges during each vibration cycle.

In [6] contact forces are represented by a line-force on the cylindrical contact, and by means of a surface discretized into a large number of contact elements on the opposite flat-to-flat contact. At each contact element, a Coulomb slider is introduced with both tangential and normal stiffness, the latter non-linear to take into account the roughness according to an Abbott model.

A common feature of most of the papers from the initial stages up to today is that of developing and proposing their own calculation method of a complete blade-dampers or disk-blade-dampers system in the form of a dedicated [7, 9] or proprietary software, as DATAR [6,12], FORSE [14], NOVA, the last used in papers as [15] that demonstrate the capability of simulating nonlinear responses of bladed disks with mistuning.

Paper [7] proposes a general method for nonlinear forced response analysis for bladed discs with friction dampers

of different designs. This contribution represents a departure from the approaches previously examined. It is based on the explicit modelling of friction dampers in the analysis of the nonlinear forced response of bladed discs, utilising large-scale high-fidelity finite element (FE) models. This paper presents numerical studies of realistic bladed discs with three different types of UDs: a "cottage roof" (wedge) damper, a seal wire damper, and a ribbon damper.

The increasing complexity of geometry and parameters has led to an objective need to keep computational time below values that tend to become prohibitive. This occurs in the computationally intensive problems encountered in practical applications to turbine blades equipped with damping devices, when it is necessary to systematically explore a design space [9, 13, 14].

In [9] the robustness of the optimal blade-damper coupling is treated through a probabilistic approach. It takes into account uncertainties in the friction coefficient, excitation level and linear damping, applied to a rotationally periodic assembly of a bladed disk with UDs. The computational efficiency of nonlinear dynamic analysis is achieved by employing a reduced-order parametric model (ROM) based on nonlinear vibration modes. This proof-of-concept study uses an academic geometry with beams in pure bending integral with a perfectly tuned disk, and rigid body UDs of the cottage-roof type.

The analysis of the blade-damper coupling performed in [13] is deployed in design space defined by ten geometric parameters of damper, neck and airfoil. An asymmetric contact damper is modeled by FEA but maintaining only rigid body DOFs. In order to keep the calculation time within reasonable limits, the exploration of the parameter space and the subsequent calculation of the performance (in terms of high cycle fatigue) is carried out via a three-level DOE sampling producing a response surface for the first bending mode.

In [14] the issues of damping performance, resonant frequency stability and robustness are addressed for a symmetric wedge damper coupled to the blade pair of an academic "two blades" test-rig, all modeled using FEM. The search for the optimal design is done via a surrogate model. The design space includes three variables, one of which (the platform groove angle) has simulated uncertainties due to manufacturing tolerances, which implies the recognized possibility of edge contacts. Similar to [12], only the first bending mode is studied.

In the meantime, POLITO's AERMEC Lab. pursued the development of experimental and numerical methods to deal with nonlinear problems related to bladed disks with any kind of dry friction damping. In UD application it is used to tune contact parameters, develop criteria for damper optimization and for damper-blade matching.

This agenda was developed at AERMEC Lab., during the last 15 years or so, along the following lines:

1. development of a first non-resonant test-rig measure simultaneously the resultant forces exchanged between a damper and the two simulated adjacent platforms, together with their absolute and relative kinematics
2. determination of contact parameters (coefficient of friction, stiffness) based on the shape of the measured hysteresis loop, as opposed to parameter tuning techniques based on numerical-experimental comparison of FRFs deemed insufficient,
3. development of a second improved test-rig towards the simultaneous measurement of tangential force and sliding directly at the damper-platform contact surfaces, to achieve highest reliability on values for tangential contact stiffness and friction coefficient,
4. adoption of an asymmetric-contact damper (flat to flat and cylindrical), evolved into a three-point damper, as opposed to the “cottage-roof” or wedge damper, to ensure full control of the position of the resultant contact forces on both sides of the damper.

Line 1 was approached with the first non-resonant test-rig, [10], which allowed us to determine the forces exchanged at the damper-platform contacts simultaneously with the absolute movements of the damper and simulated platforms.

Line 2 was addressed first in [10] by manual tuning, later in [19] with a Latin Hypercube sampling technique, in both cases for a laboratory three contact damper and with some limitation on the number of independent contact parameters. This required either hypotheses on the ratio of normal to tangential stiffness, or independent measurements of friction and stiffness made on purposely dedicated test-rigs [20, 21]. A special application is found in [22], where a special laboratory crossed curve-flat damper subjected to In-Phase vibrations was used to extract from the hysteresis cycle the two friction coefficients and two pairs of contact stiffness values, normal and tangential, on either contact surface. Contrary to other methods available at that time, the values of contact parameters were derived solely from experimental data, without support from other analytical or numerical sources.

Line 3 was addressed in [23], where an extension to [10] was applied by introducing new sets of experimental evidence (hysteresis cycles at the contacts and moment vs rotation diagram) to uniquely estimate the contact stiffness values on a Siemens type contact-asymmetric damper. Paper [24] presented a new test-rig with several advanced features, probably the most sophisticated collection of normal and tangential stiffness measurements for the time, for both cylindrical and flat-to-flat contacts. With these tools the problem of erratic behaviors due to machining imperfections on the plane contact surfaces of the damper was addressed [24].

Line 4 represents a significant divergence from other schools of thought, encompassing two distinct issues.

- whether it is more appropriate to introduce the plane-on-plane discretized contact surface into the numerical model, or whether it would be more rational to treat the resultant force directly.
- whether a simpler wedge geometry of the damper or an asymmetric contact geometry is preferable.

Regarding the first issue, the determination of plane-on-plane contact forces by full FEM discretization of the contact surface is a most often preferred practice, for instance [7, 9, 12, 14, 25, 26]. However, it should be observed that in the case of a contact-asymmetric damper, [6, 18], the line contact on one side implies that the position of the resultant force on the opposite flat-on-flat contact is automatically determined independently of the pressure distribution. Based on this, the position at AERMEC has always been to pre-determine the position of resultant forces on a rigid body model of a contact-asymmetric damper, both experimentally and numerically, as in [10, 13, 16, 27, 28, 29].

This opens up the second issue, for which [18] is exemplary in stating that:

- for dampers to be effective, a sliding full contact between the damper and platform surfaces must be maintained for any combination of tangential and radial relative platform motions,
- in order to avoid a rocking motion, that would significantly reduce the effectiveness of the damper in dissipating the vibrational energy, the damper should have raised bearing surfaces (pads) around the points where contact is precisely desired,

It was observed [24], that these pads or reliefs are highly suggested on the plane extended contact (left side of Fig. 2) even in the case of In-Phase vibrations for an additional reason: the lack of flatness due to machining, even within tolerances, may be the origin of extremely erratic force-displacement cycles, as stressed in [6, 24] but anticipated already in [1].

In the case of Out-of-Phase vibrations, as well as in the case of In-Phase vibrations with a non-zero interblade phase-angle, a wedge damper suffers edge contacts and liftoff, while instead an asymmetric-contact damper is always self-aligning within platforms in all possible cases [16, Appendix 2].

Other laboratories however follow different lines to investigate the effect of the contact surface area on the damping capacity. For instance, the two-blade test-rig is revived by [12], while a three-blade scheme is used in [25]. Paper [12] adopts an explicit model of the damper, equipped on the contact surfaces with a dense grid of 3D contact friction elements, in combination with multi-harmonic balance solvers, and validates the numerical solutions with the test-rig. It is found that the results are strongly dependent on the pressure distribution on the contact surfaces, and therefore detects the shape of those of the damper which in fact turn out to be slightly convex due to the manufacturing process. Using pressure distribution results from a pressure film, [12] finds a better agreement between numerical predictions of the FRF and experimental results.

An observation regarding the contact surface: for method validation it makes sense to detect the shape of the actual surfaces, but from a practical engineering point of view it seems more appropriate to avoid the problem (e. g., with raised pads) rather than reproduce it numerically.

Furthermore, in the case of [12] the angle at the vertex of the damper, although not indicated, seems to be around 120°, which combined with a declared friction coefficient of 0.6 guarantees, to this author's experience, damper rocking in IP vibration.

The Platform Centred Reduction [27] has recently been proposed, with the Base-Cycle concept [28] supplementing it. The latter refers to the cycle with the smallest amplitude of platform oscillation in which all contact forces travel a complete oscillation between the two friction limit angles, that is to say, they reach at least the onset of slip at both ends. In [16], it was demonstrated that the Base-Cycle is a unique characterization of a given damper shape. Once produced for a convenient reference case, it can be scaled linearly without recalculation according to size, radial force,

platform proportions, and proportional variation of contact stiffness.

In [28,29], the damper is represented by a complex spring, function of the relative rotation between platforms, and disappears as a physical body. The final achievement is the Amplitude Layered (Excitation) Force Mapping [29], which reduces the amount of computation by up to three orders of magnitude in comparison to standard techniques, thus making it a suitable competitor in the case of optimisations that are numerically intensive.

2 Background

This paper is the completion of a previous work [16] in which a piecewise-linear algorithm was developed for direct calculation of the hysteresis cycle of UDs. The reader should refer to [16] for the complete set of kinematic and equilibrium equations, for the treatment of the contact model and for the solution procedure.

Aim of the "parent" paper [16] were the concepts of "force Base-Cycle" that uniquely characterizes a given damper shape, and of "moment Base-Cycle" characterizing the damper coupled to a given platform.

The algorithm was applied to an example damper shape. It was demonstrated in that once produced for a convenient Reference Case, Base-Cycles can be scaled without recalculation according to damper size, radial force intensity, platform proportions, and proportional variation of contact stiffness values.

The goal of this paper is now to fill in the missing part, that is, to study how the basic cycles change with the shape of the damper, to present the different computational problems that different shapes entail, and finally to address the evaluation of shape-related damping effectiveness through appropriate indicators.

As in [16], object of this study is the contact-asymmetric UD, Fig. 1 and 2.

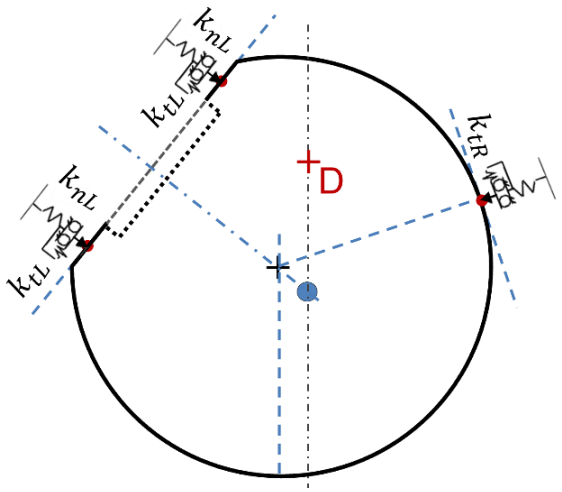

Fig. 1: SIEMENS type damper [6], represented with Jenkins discrete contact elements, dotted lines added [16] to suggest raised pads.

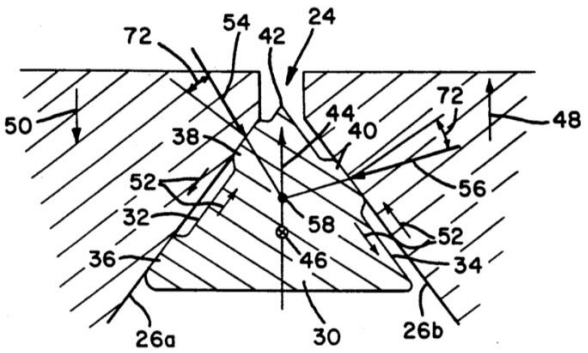

Fig. 2: From UNITED STATES PATENT N. 5,156,528, Oct. 20 1992 [15]; 48 and 50: radial motions of respect. right and left platforms

In both cases, contacts are localized by means of raised pads, each accommodating a Jenkins contact element, one on the right and two at the flat-on-flat surface on the left.

All dampers of the types of Fig. 1 and 2 belong to the same family of geometries and therefore are best described [16] according to Fig. 3. In brief:

- the vertical reference line passes through the center of mass (not shown) of the damper, on which its radial centrifugal force F_D acts
- the line through point L, the midpoint of segment L_1 - L_2, is the main horizontal reference line
- these two reference lines cross at a point D, named the "damper reference point"
- point L (in section) has the role of "left surface reference point"
- the intersection of the horizontal reference line with the line tangent to the right contact in R_1 is named R, the "right surface reference point"
- the three reference points (L, D, R) are then aligned horizontally
- the Jenkins contact elements act on points L_1, L_2, R_1

- in order to precisely locate the contacts, it is possible either to adequately limit the pad width or, in addition, to locally impart a (large) radius of curvature thus realizing a cylindrical Hertzian contact.

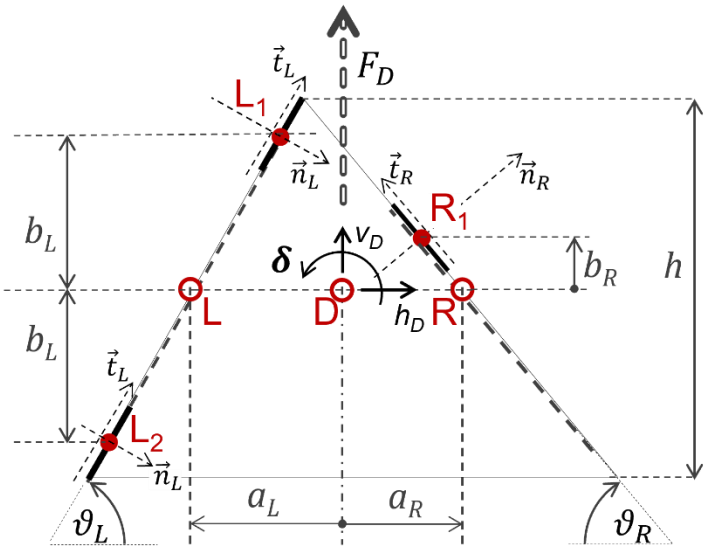

Fig. 3: Geometry preferred in [1] to describe the contact-asymmetric damper

An advantage of the solution of Fig. 2 over that of Fig. 1 is the free adjustment of the position of R_1 with respect to R, i.e., freedom to choose the value of b_R. This paper shows how to take maximum advantage of this freedom.

In [16] it was first demonstrated that the relative motion of damper and adjacent blade platforms can be reduced to a kinematically equivalent system of parallel blades: Fig. 4 shows schematically the damper type of Fig. 2 between the adjacent platforms that rotate about their "instantaneous velocity center" C about which the platform has a pure rigid rotation. On the right the position of maximum clockwise rotation, corresponding to what will be named the cycle's point 0, and on the left the maximum counterclockwise rotation, corresponding to the cycle's point C. Note that the relative motion represented in Fig. 4b is the same indicated by vertical platform displacements 48, 50 of Fig. 2, where the corresponding relative sliding motions between damper and platforms are indicated as 52.

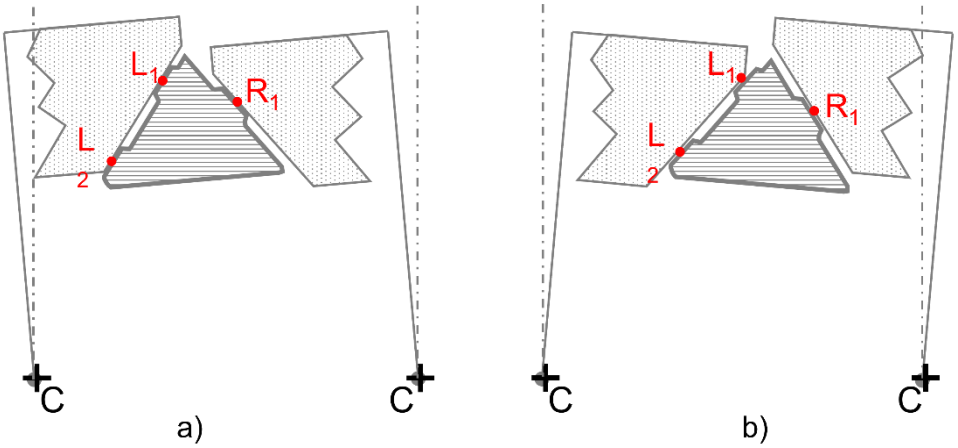

Fig. 4: In-Phase vibration, platforms rigidly rotating about their "instantaneous velocity center" C; a): max counter-clockwise rotation; b): max clockwise rotation.

As shown in [16], the number of linear tracts of the piecewise solution is equal, for each half-cycle, to the number of the contact points where the contact Jenkins elements are applied. They correspond to the number of stick-slip transitions. However, this paper will show that there are exceptions to this simple rule.

The equilibrium equations of the damper give origin [16] to a damper "force" cycle, i.e. the cycle of contact forces applied to the damper during the motion of platforms. Once the damper "force" cycle is known, a platform "moment" cycle is calculated, i.e., the moment produced by contact forces on the platform versus the angle of rotation of the

platform.

In [27], the concept of Platform Centered Reduction was introduced, in which the number of non-linear DOFs was reduced to those of a rigid body for both platform and damper, followed in [28] by that of "Base-Cycle," defined as follows:

"Base-Cycle: the cycle established at the smallest platform oscillation amplitude at which all contacts reach the slip condition at both ends of the oscillation"

The concept of Base-Cycle holds for both the damper "force" cycle and for the platform "moment" cycle. In this case, the DOFs of the damper are eliminated from the dynamic equations of the damper-blade system, and replaced by the platform "moment" cycle, in [16] a function of the In-Phase oscillation amplitude of the platform in Mode 1, Fig. 5.

In [16] it is demonstrated that the damper "force" Base-Cycle, during In-Phase vibration, is a function uniquely of the difference $(\boldsymbol{v}_{DL} - \boldsymbol{v}_{DR})$ of the radial, i.e. vertical displacements (Fig. 6) $\boldsymbol{v}_{PL}$, $\boldsymbol{v}_{PR}$ of respectively a left point D_{PL} and a right point D_{PR} , both placed in the same geometric position as the damper reference point D, but belonging to, and moving with, the left (L) and right (R) platform. Distance q^* is the "virtual" pitch, defined in [16], of parallel blades kinematically equivalent to the real blades that have a relative angular pitch 2β, Fig. 5.

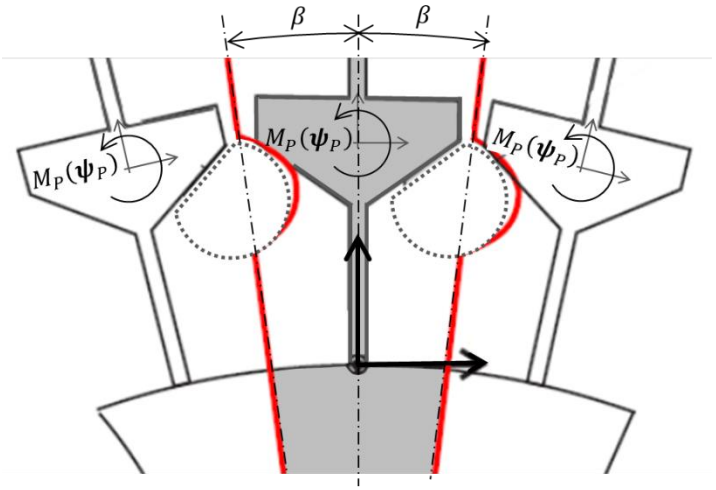

Fig. 5: Moment M_P applied to the platform by the two adjacent dampers, function of the damper rotation ψ_P

A final concept imported here from [16] is that from the platform "moment Base-Cycle", any other cycle having higher amplitude of platform rotation can be deduced by means of a simple "constant moment" stretch, or amplitude elongation, in full-slip. Then, the diagram of the real and imaginary parts (HBM) of the complex stiffness applied to the platform, dynamically equivalent to the friction contact forces, is trivially calculated for any platform vibration amplitude. Then, there is no need to iterate the cycle calculation as in the customary HBM-AFT procedure [28, 29].

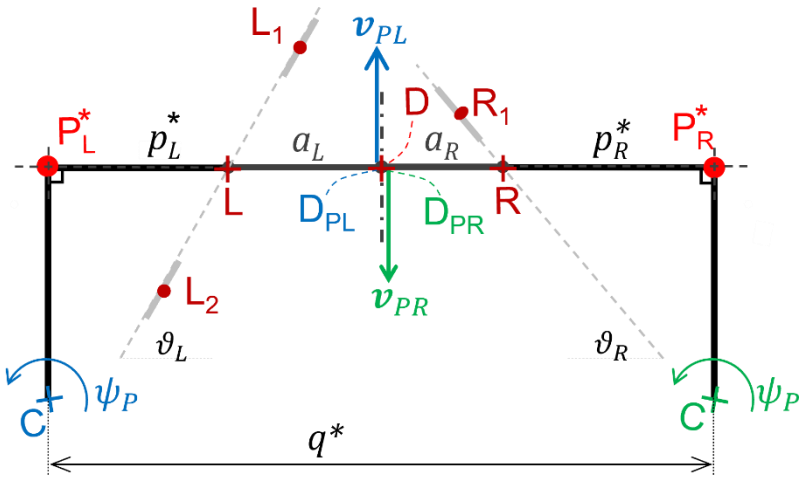

Fig. 6: Hemi-platforms displacements of their fictitious ends D_{PL} and D_{PR} in D due to a clockwise In-Phase platform rotation,

when $\boldsymbol{v}_{PR}$ moves upwards and $\boldsymbol{v}_{PL}$ is specularly opposite

3 The Method Illustrated on the Shape-Case 60sym

The main purpose of this section is to acquaint the reader with all the graphs representing the behavior of the dampers, commenting on them extensively to facilitate the reader's understanding. It concludes by stating-in summary-the minimum set of data that, once the method is acquired, is necessary and sufficient to fully characterize a damper-platform coupling.

This section deals with the symmetrical (however, contact asymmetrical) damper with input parameters (Fig. 3):

ϑ_L=60°, ϑ_R=60° (1.a)
$2b_L$=0.8 h (1.b)
$b_R\,/h$ =0.14 (1.c)

The friction coefficient at three levels (μ = 0.3 ; 0.5 ; 0.7) the lowest being the most likely at the highest temperatures while the highest being possible in cold start conditions.

Assumption (1.b) means that the centers of the left pads, L_1 and L_2, are the ends of an L_1-L_2 segment that represents 80% of the total available left flank. The extension of each pad in cross section is then 20% of the left flank. This assumption is common to all dampers considered in this study.

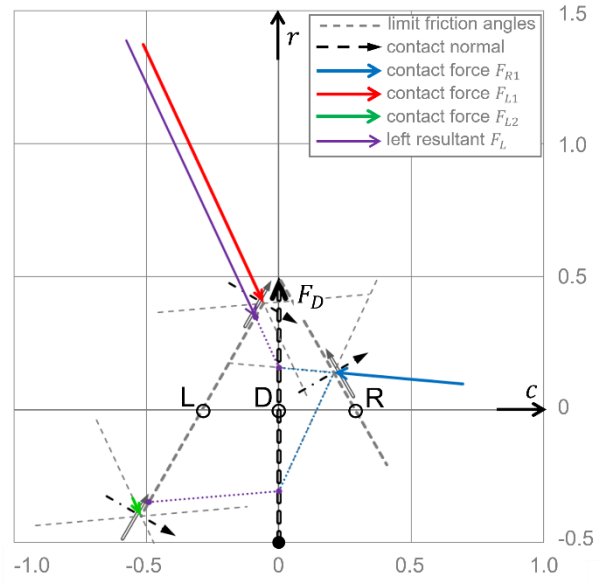

Fig. 7a: 60sym cycle-start, μ = 0.7 : full-slip at the end of clockwise platform rotation, i.e., relative motion as in Fig. 2 and Fig. 4 right

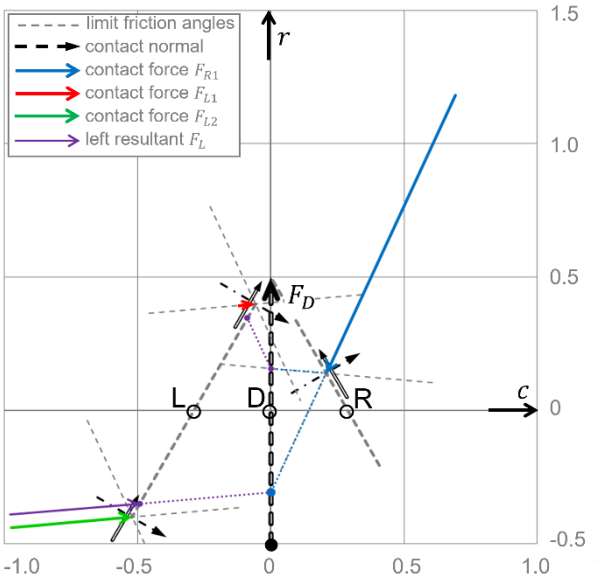

Fig. 7b: 60sym mid-cycle, μ = 0.7 : full-slip at the end of counter-clockwise platform rotation, , relative motion opposite to that of Fig. 2 and Fig. 4 left

Assumption (1.c) for the positioning of point R_1, i.e., for the choice of the value of $b_R\,/h$ =0.14 (discretization to second decimal place), comes from imposing that with the highest possible coefficient of friction ($\mu = 0.7$) the left resultant force at the two extreme positions, at the beginning of the cycle and at mid-cycle respectively, falls at the same distance from the nearest contact point and inside the L_1-L_2 segment. In this case the distance of the resultant force from L_1 is 6.6% of $\overline{L_1\text{-}L_2}$ and that of L_2 6.5%. So as to ensure no liftoff, or, as said in [18]: "*such as to preclude rotating or rocking … … for conditions of maximum coefficient of friction*".

Figures 7a,b show the case for μ = 0.7, cycle-start and mid-cycle. Geometric dimensions are normalized to the value of h, i.e., $h = 1$. Forces normalized to the centrifugal force $F_D = 1$. Radial and circumferential directions respectively r and c. Figures 7a,b represent full-slip conditions, i.e, all contact forces are at their limit friction angles, indicated by the dashed lines on either side of the contact normal. Dotted lines represent the lines of action of the resultant forces that cross on the line of action of the centrifugal force.

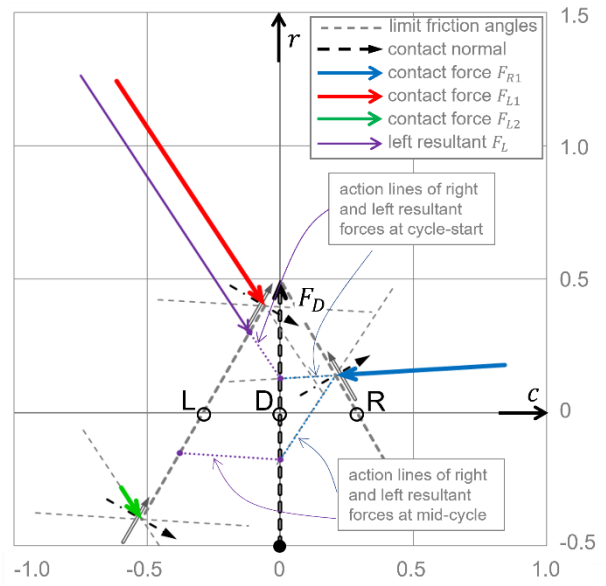

Fig. 8a: 60sym cycle-start, full-slip, μ = 0.5

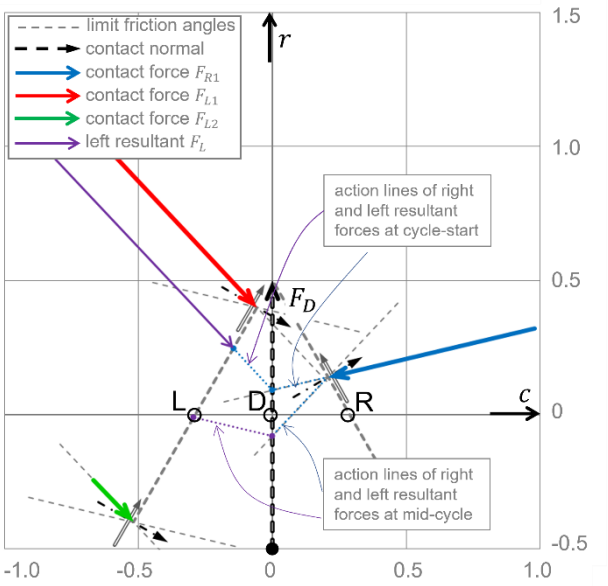

Fig. 8b: 60sym cycle-start, full-slip, μ = 0.3

Figures 8a,b show the equivalent of Fig. 7a for, respectively, μ = 0.5 and μ = 0.3, keeping b_R/h =0.14. Although only the cycle-start condition is represented, lines of action of the right and left resultant forces are represented by dotted lines for both cycle-start and mid-cycle. Table 1 collects the distances of the left resultant force to the nearest left contact (L_1 or L_2, Fig. 3) in % of $\overline{L_1\text{-}L_2}$ during the cycle, consequence of the design decision to adopt the value of b_R/h that guarantees equal distance for the highest predicted friction angle μ = 0.7.

Table 1: 60sym distances of resultant left force from nearest contact, in % of $\overline{L_1\text{-}L_2}$.

Friction coeff. μ	dist. from L_1	dist. from L_2
0.7*	6.6%	6.5%
0.5*	12.3%	31.0%
0.3*	19.2%	48.7%

* b_R/h =0.14

Fig. 9a displays the equilibrium polygon of centrifugal force and contact forces at the cycle-start of Fig. 7a. Fig. 9b displays the force increments between cycle-start (point 0, corresponding to Fig. 4 right) and the end of the first tract (point A), covered during the counter-clockwise (reverse motion) platform rotation with all contacts still in stick.

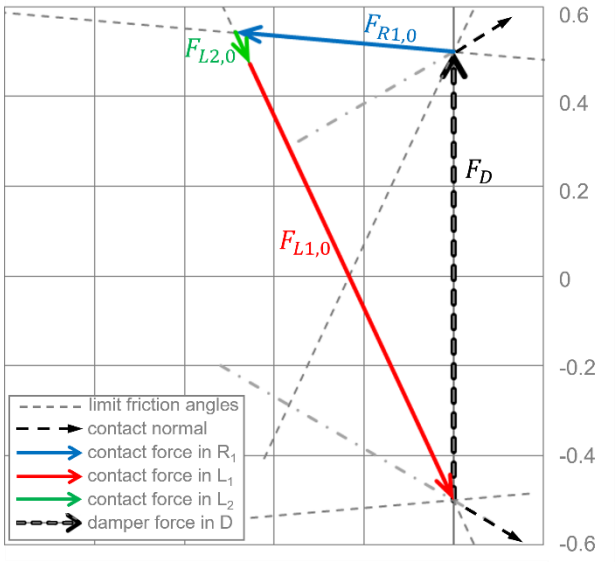

Fig. 9a: 60sym forces on damper according to Fig. 6a, cycle-start, point **0**, normalized $F_D = 1$

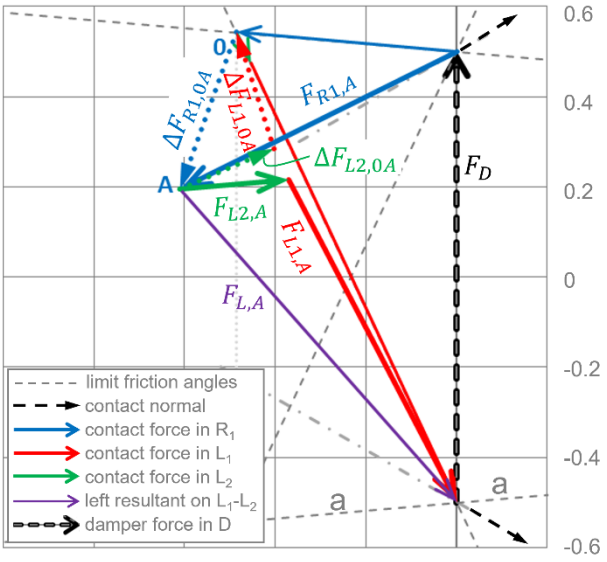

Fig. 9b: 60sym increment from cycle-start, point 0, to end of first tract, point **A**, normalized $F_D = 1$

Dotted vectors are the force increments $\Delta F_{R1,0A}$, $\Delta F_{L1,0A}$, $\Delta F_{L2,0A}$ that summed to the contact forces $F_{R1,0}, F_{L1,0}, F_{L2,0}$ give the final contact forces $F_{R1,A}, F_{L1,A}, F_{L2,A}$, hence also the left resultant $F_{L,A}$.

Notice that the final force $F_{L2,A}$ is parallel to the friction boundary line a-a, i.e., in the contact L_2 the transition for stick-to-slip is realized: consistent with the fact that, [16], the cycle is calculated by succession of linear tracts, each of which ends with a stick-to-slip transition at one of the contact points.

The complete collection of figures following 0-A to E-F (F=0) is summarized as an "equilibrium track" by Fig. 10a, named also "force Base-Cycle" of the damper, where the blue thick-line closed loop indicates the path of the tip of the vector F_{R1} as well as the tail of the vector F_L . The secondary loop, thin red dashed line, indicating the path of the tail of the vector F_{L1} can also (if necessary) be represented. The "force Base-Cycle" is represented normalized to F_D=1.

The value of this figure lies in the fact that it contains all the information about the positions of the contact forces during the Base-Cycle as they travel through the space between the friction boundary angles. In addition, this polygonal figure is uniquely related to the damper shape and friction coefficient, and contains all the information necessary for the subsequent calculation of the Base-Cycle moment.

Fig. 10b collects the three equilibrium tracks for μ = 0.7; 0.5; 0.3. To be remarked that in for all friction coefficients the cycle closes at the end of the first sequence of tracts, i.e., **F≡0** exactly at the end of the last tract. At the and of tract **E-F** the last contact in stick, here R_1, becomes slip when the backward half-cycle is completed and the initial position reached.

Complementary to this figure, Table 2 tracks the succession of transitions that take place in the tracts. For instance, for the 60sym damper, at the end of tract 0-A contact L_2 reaches full-slip, then it is maintained during the following tract A-B, and so on. At point C there is full-slip on all contacts and motion reversal. Point F coincides with point 0. Note that tract D-E does not have the same transitions for all values of μ.

Comparing rows **B-C** and **E-F** of Table 2 with Fig. 10b one can check that tracts **B-C** and **E-F** are effectively on the left friction angle, as contacts L_1 and L_2 are in slip.

Table 2: Shape-case 60sym: Transitions Chart, stick or slip condition at contacts in cycle tracts

	μ = 0.7		μ = 0.5		μ = 0.3	
tract	**in stick**	**in slip**	**in stick**	**in slip**	**in stick**	**in slip**
0-A	$R_1 L_1 L_2$		$R_1 L_1 L_2$		$R_1 L_1 L_2$	
A-B	$R_1 L_1$	L_2	$R_1 L_1$	L_2	$R_1 L_1$	L_2
B-C	R_1	$L_1 L_2$	R_1	$L_1 L_2$	R_1	$L_1 L_2$
C-D	$R_1 L_1 L_2$		$R_1 L_1 L_2$		$R_1 L_1 L_2$	
D-E	$R_1 L_2$	L_1	$R_1 L_1$	L_2	$R_1 L_1$	L_2
E-F	R_1	$L_1 L_2$	R_1	$L_1 L_2$	R_1	$L_1 L_2$

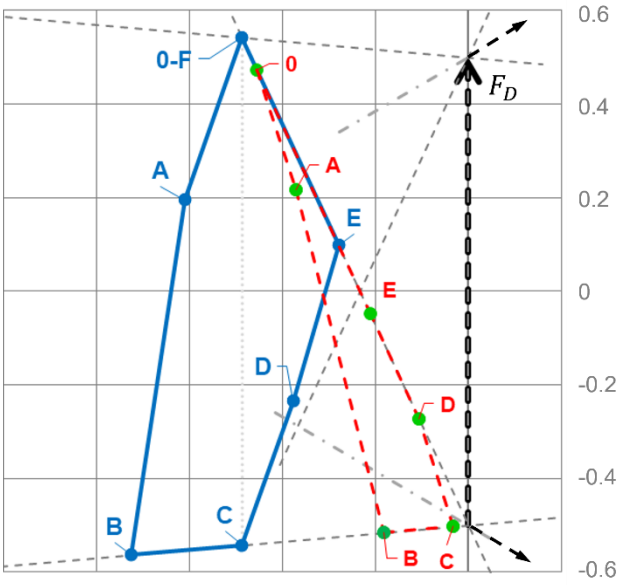

Fig. 10a: 60sym, μ = 0.7: equilibrium track, or normalized "force Base-Cycle" (solid blue: equilibrium track; thin dashed red: secondary loop)

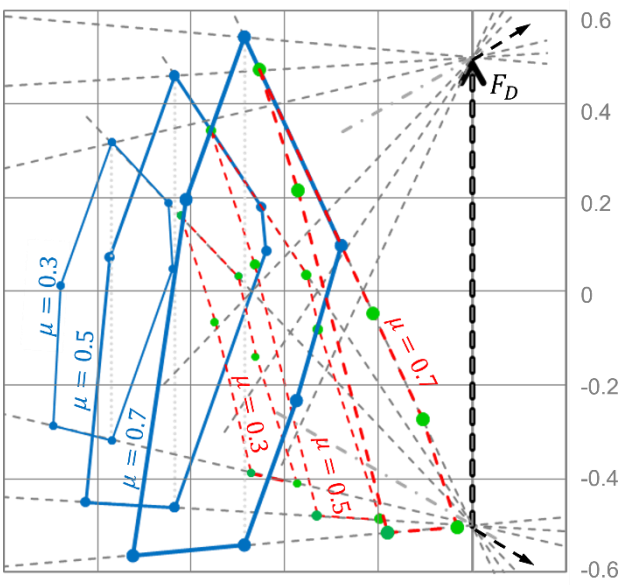

Fig. 10b: 60sym, μ = 0.7, 0.5, 0.3: equilibrium tracks or normalized "force Base-Cycles" (solid blue: equilibrium tracks; thin dashed red: secondary loops)

The "moment Base-Cycle" is then defined as the cycle of the moment M_P applied to the platform by the damper-to-platform forces versus the platform rotation angle ψ_P , Figs. 5, 6. The moment is calculated point by point (0, A … to F) according to the general schemes of Figs. 11, 11 (details in [16]), its value being:

$$M_P = \left(F_{L,v} - F_{R,v}\right)\left(q^*/2 + r \ \sin\beta\right) \tag{2}$$

Data from the "force" Base-Cycle, Fig. 10a,b , are transformed into the "moment Base-Cycle", that in Fig. 12 is represented as moment M_P vs. platform relative displacement $(v_{DR} - v_{DL})$ and platforms' rotation angle ψ_P , related by:

$$\psi_P \ = \ (v_{DR} - v_{DL}) \ / \ q^* \tag{3}$$

Unlike the normalized "force Base-Cycle" of Fig. 10a,b exclusively connected to the damper's shape and the friction coefficient, the "moment Base-Cycle" will be here expressed for a Reference Case where damper radial force and virtual blade pitch are assumed as:

F_D = 1000 N (4.a)
q^* = 100 mm (4.b)

Fig. 13 shows the "moment Base-Cycles" for μ = 0.7; 0.5; 0.3 . Any other case is obtained from a "Reference Case" by proportional scaling. The rules for scaling according to geometry and proportional change of all contact stiffness values from the "Reference Case" to any other case are given in [16].

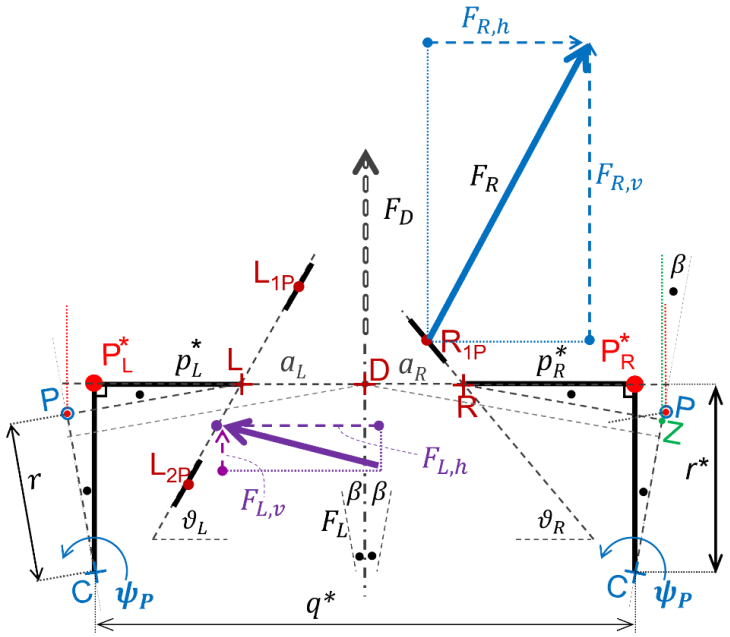

Fig. 11: Geometric scheme for the calculation of platform moment about point P, according to [16], in terms of resultant forces

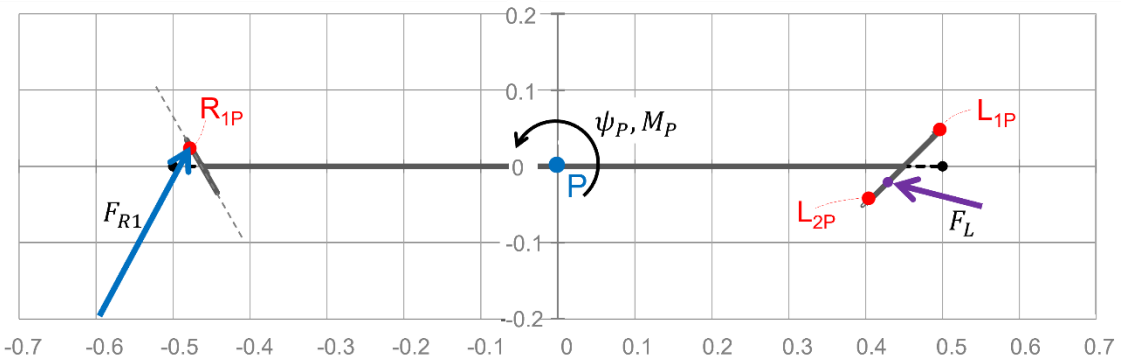

Fig. 12: Platform non-dimensionalized for q^*=1, scheme of contact forces producing moment about P

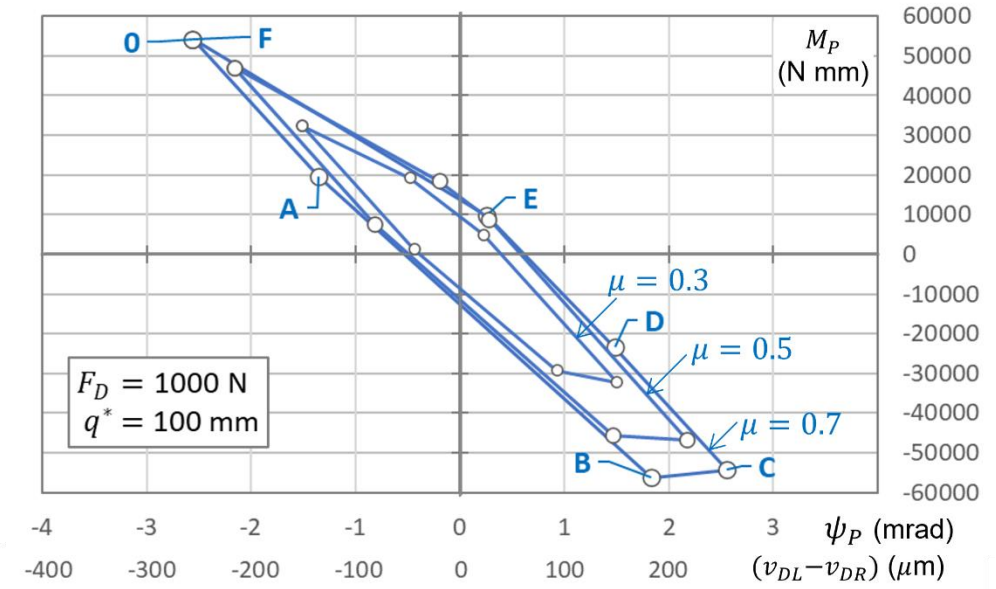

Fig. 13: Case 60sym, μ = 0.7, 0.5, 0.3: "moment Base-Cycle": moment M_P on platform vs. platforms' relative vertical displacement $(v_{DL} - v_{DR})$ and, by way of example, platform rotation angle ψ_P for q^*=100 mm

Once the "moment Base-Cycle" is known, larger oscillation amplitudes stretch it horizontally as Fig. 14, where an increasingly larger portion of the platform rotation in both directions is spent in full-slip at all contact points. In the diagram, point 0-F and point C of Fig. 13 are now split into pairs 0-F and pairs C-C' in Fig. 14, respectively, the ascending and descending half-cycles shifted to the left and right, respectively, so as to obtain the desired amplitude of rotation $\psi_{P,a}$ larger than that of the Base-Cycle. Fig. 14 shows the cases $\psi_{P,a}$ = 3, 4 and 6 mrad, and splitted points are given names, for clarity, only on the cycle $\psi_{P,a}$ = 6 mrad.

In Fig. 14 each cycle is accompanied by its Fourier representation that to the purpose of damping the first bending mode can limited to the first order [27, 28].

Finally, from this representation the function $M_P\,(\psi_P)$ is written as a complex number:

$$\overline{M_{P,a}} = \bar{k}\ \psi_{P,a} \tag{5}$$

where the complex stiffness:

$$\bar{k} = k_{Re} + i\,k_{Im} \tag{6}$$

has the real and imaginary parts (k_{Re}, k_{Im}), represented in Fig. 15 for all amplitudes: $\psi_{P,a}$ larger than the Base-Cycle amplitude $\psi_{P,a,Base-Cycle}$ that in this case is found at the value 2.56 mrad.

In Fig. 15 are also indicated the amplitude of the largest cycle in full-stick, amounting here at $\psi_{P,a}$ = 0.60 mrad, and the value of the corresponding real rotational stiffness on the platform due to the constraint of the adjacent dampers, here at 28741 (Nm /mrad). In this range the value of the imaginary component, related to damping, is obviously zero.

The interval between the end of the full-stick, $\psi_{P,a}$ = 0.60 mrad, and the onset of full-slip, $\psi_{P,a}$ = 2.56 mrad, is a zone of multiple solutions that depends on the initial equilibrium of the damper between the two adjacent platforms, and is not an objective pursued in this paper whose purpose is the determination of the maximum damping characteristic of a damper shape.

The Base-Cycle is represented by the amplitude $\psi_{P,a}$ = 2.56 mrad, the associated real and imaginary stiffness coefficients, 21679 and 4583 N mm / mrad respectively, that are the basis to calculate the values for larger amplitudes [16].

In conclusion, it should be emphasized that in order to construct the curves in Fig. 15 - which are used to calculate the best match of a given damper to the given blade - it is sufficient to have five numbers (values for the present example provided for easy recognition):

1. the "Base-Cycle" oscillation amplitude (here at $\psi_{P,a} = 2.56$ mrad)
2. the corresponding values of $k_{Re}$and k_{Im} (here at 21679 and 4583 N mm / mrad)
3. the "full-stick" maximum oscillation amplitude (here at $\psi_{P,a} = 0.60$ mrad)
4. the corresponding value of the initial k_{Re} (here at 28741 N mm / mrad)

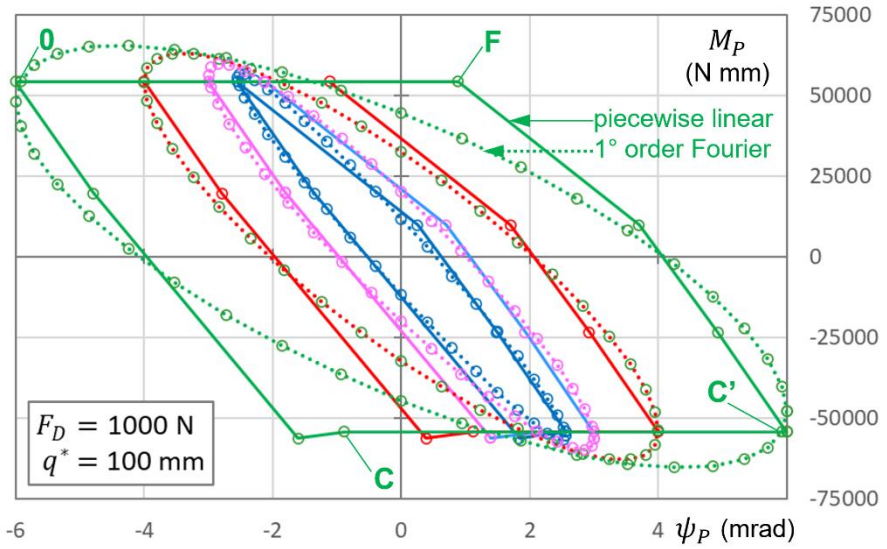

Fig. 14: Case 60sym, μ = 0.7: M_P vs. ψ_P. Moment Base-Cycle, ψ_{Pa}= 2.56 mrad (blue) and examples of stretched BCs (ψ_{Pa}= 3, 4, 6) mrad (respectively: violet, red, green). Solid lines: Base-Cycles. Dotted lines: their first-order Fourier representations. On the largest, 0-F = C-C' is the full-slip stretching.

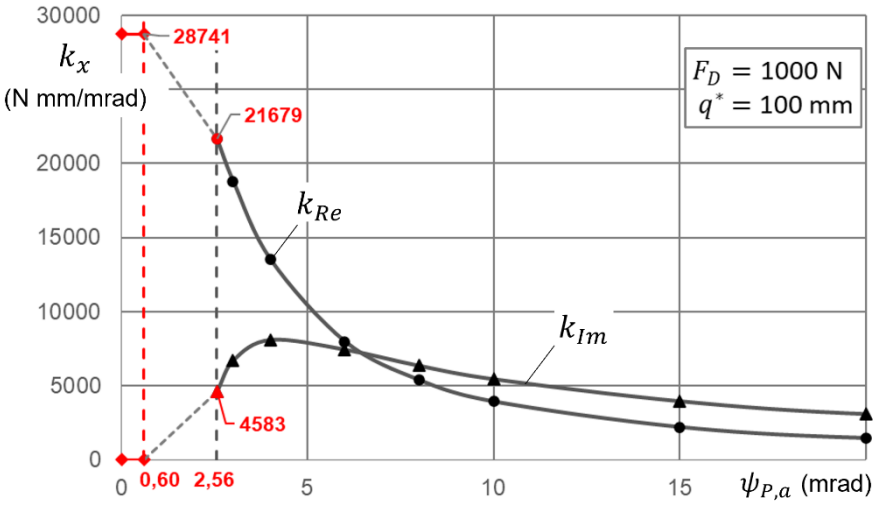

Fig. 15: Case 60sym, μ = 0.7, real, k_{Re} , and imaginary, k_{Im} (N mm/mrad) components of platform rotational stiffness vs. amplitude of alternating platform rotation $\psi_{P,a}$ (mrad)

The microslip range $0.60 < \psi_{P,a} < 2.56$ is briefly commented. Whenever the damper is unable to reach generalized gross slip at all contacts, different initial states at contacts give rise to great variability in vibration amplitudes and resonance frequencies, as confirmed experimentally by [30, 31]. In [32], a numerical method for calculating the response limits of systems with friction contacts is proposed, based on a constrained optimization to search for a configuration that maximizes or minimizes the system's loss factor.

Whatever the approach, in the microslip range the values of real or imaginary stiffness depend on the non-unique initial state. In [30] it is observed that the "… *inability of a damper to reach generalized gross slip for the expected forcing levels is doubly harmful: not only its damping capability is reduced but the range of possible dynamic responses increases. Therefore, one of the UD design priorities should be to tailor the damper shape and mass to the blade mode shape in order to ensure that generalized gross slip is easily reached.*"

It therefore seems logical to pursue the lowest possible value of the rotation $\psi_{P,a}$ at which Base-Cycle (i.e., onset of full slip at both cycle ends), together with the highest possible value of the corresponding k_{Im} .

Damping in the microslip field is not the subject of this paper, the purpose of which is to determine the maximum damping performance. As commented above on Fig. 15, calculation of such cycles starting with loading history dependent initial state is the object of a specific approach, as in [32]. In the present context, linear interpolation (dashed line) can be considered an indication of the achievable complex stiffness.

4 Case Shape-Case 45sym

In the case of the 45sym shape this is impossible to obtain a valid solution (no liftoff, no damper rolling) for μ = 0.7, as shown in Fig. 16 for the position of point R_1 (points R_1, L_1, L_2: Fig. 3). If (by way of example) we choose b_R/h = -0.20 so that the position of the resultant force on the left at cycle-start is slightly below L_1 (distance to L_1 2.94% of $\overline{L_1\text{-}L_2}$, the left resultant at mid-cycle is completely out of segment L_1-L_2 , over 3,8 times $\overline{L_1\text{-}L_2}$. In this case the strategy of setting b_R/h for μ = 0.7 must be abandoned.

Fig. 17a shows the optimal position of R_1 for μ = 0.5, with b_R/h = 0.20. However, should the contact move slightly above or below this optimum position, for μ = 0.5 the damper is at high risk of rolling and liftoff, see Table 3. When μ = 0.3, b_R/h = 0.20, Fig. 17b, the damper is obviously at no risk of liftoff.

Overall, considering the marginal safety conditions against rolling, this damper geometry is not recommended and will not be analyzed further. The rest of the paper examines the family of damper shapes derived from the 60sym.

Table 3: case 45sym, distances of resultant left force from nearest contact, in % of $\overline{L_1\text{-}L_2}$.

Friction coeff. μ	dist. from L_1	dist. from L_2
0.7	NA	NA
0.5*	0.4%	2.5%
0.3*	7.7%	42.9%

* b_R/h =0.20

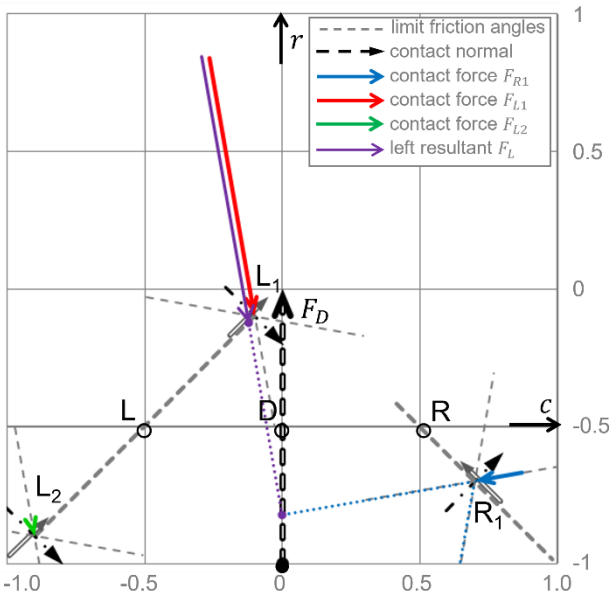

Fig. 16: 45sym cycle-start, μ = 0.7, b_R/h = - 0.20.

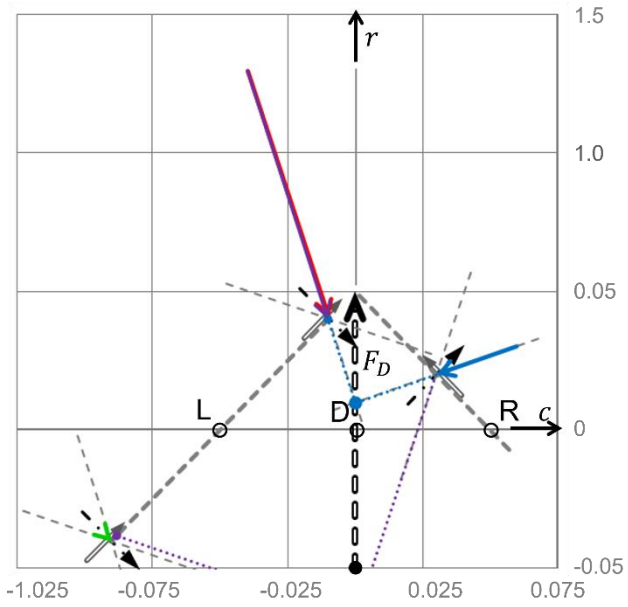

Fig. 17a: 45sym, cycle-start, full-slip, μ = 0.5, b_R/h = +0.20

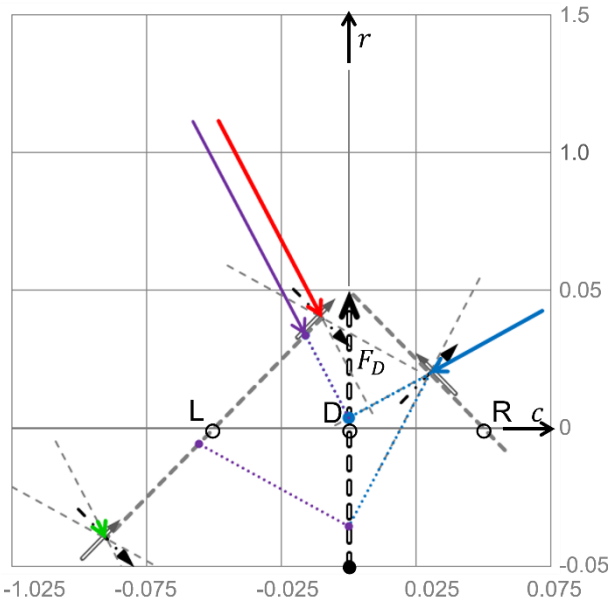

Fig. 17b: 45sym, cycle-start, full-slip, μ = 0.3, b_R/h = +0.20

5 The 60sym Family of Shapes, Comparison Criteria

The family of shapes compared in this paper is presented in Fig. 17. Shape named “60sym” is the symmetrical shape with base angles ϑ_L=60°, ϑ_R=60° already presented in Section 3. The other members of the family are obtained by moving the vertex of the triangle in steps of ¼ the base length.

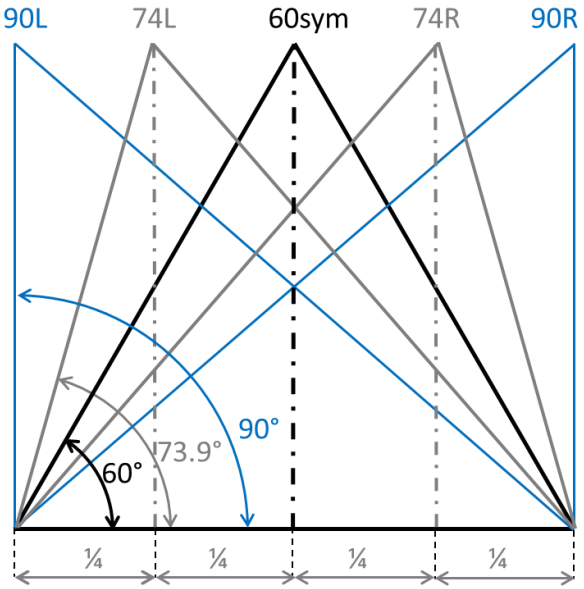

Fig. 18: The 60sym family of shapes

Shapes 90L (ϑ_L=90.0°, ϑ_R=40.9°), 74L (ϑ_L=90.00°, ϑ_R=49.1°), 74R (ϑ_L=49.1°, ϑ_R=73.9°), 90R (ϑ_L=40.9°, ϑ_R=90°) are examined comparatively together with the “parent shape” 60sym.

Sections 6 to 9 illustrate the main features of this family, except the case 60sym already presented in the “guide” Section 3. For each shape the following fundamentals are presented:

- $2b_L/h$ = 0.8 in all cases, with one small exception in Case 90L

- value of b_R/h chosen for the best left resultant force placement at μ = 0.7
- cycle-start analogue of Fig. 7a
- "force" Base-Cycles or equilibrium tracks for μ = 0.7, 0.5, 0.3, analogue of Fig. 10b
- "moment Base-Cycle", analogue of Fig. 13
- chart of transitions, analogue of Table 2, for μ = 0.7, 0.5, 0.3

plus, when necessary, illustration of **special features** on transitions and **special features** on cycle convergence.

Section 10 compares the performance characteristics of all shapes on the basis of:

- complex stiffness curves for μ = 0.7, 0.5, 0.3
- indicators of energy dissipation on contacts

6 The Shape-Case 90L

Table 4 shows the values of distances of the left resultant force from the contacts L1 and L2. The choice of $b_R/h = 0.15$ does not give, for $\mu = 0.7$, a position strictly equidistant from contact limits, however it is the best value available by rounding-off to the tenth of a millimeter.

Table 4: Shape-case 90L, distances of resultant left force from nearest contact, in % of $\overline{L_1\text{-}L_2}$.

Friction coeff. μ	dist. from L_1	dist. from L_2
0.7*°	1.2%	14,1%
0.5*	8.2%	35.3%
0.3*	18.3%	49.0%

* $b_R/h = 0.15$, °$2b_L/h = 0.85$

For $\mu = 0.7$ the vertical distance between model contact points (L_1 , L_2) was set at $2b_L = 0.85\,h$ (ref. Fig. 3), to overcome a marginal difficulty in keeping the resultant left force inside the L_1-L_2 segment. This is reasonable because the contact pad can extend on both sides of the model contact up to 10% of the total available length of the left side of the platform.

Fig. 19a indicates the position of forces at cycle-start, and their predicted at mid-cycle (dotted lines) in the hypothesis of full slip. However, in this case, as shown in Fig. 19b, the right contact force does not reach full slip, i.e. the dotted (*) position predicted in Fig. 19a - and remains in stick during the whole cycle. Compared with previous similar figures, here the scale of the forces has been reduced to contain the vectors within the figure.

Fig. 20 shows the normalized "force" Base-Cycles or equilibrium tracks for the three friction coefficients, while Fig. 21 shows the "moment Base-Cycle". Table 5 shows the stick-slip or slip-stick transitions.

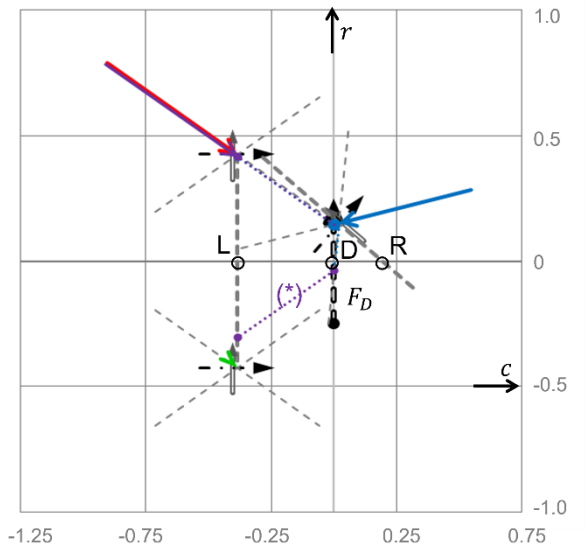

Fig. 19a: Shape-case 90L, cycle-start, μ = 0.7, force lines of action at start (up) and at predicted in full slip,mid-cycle (*) for full slip

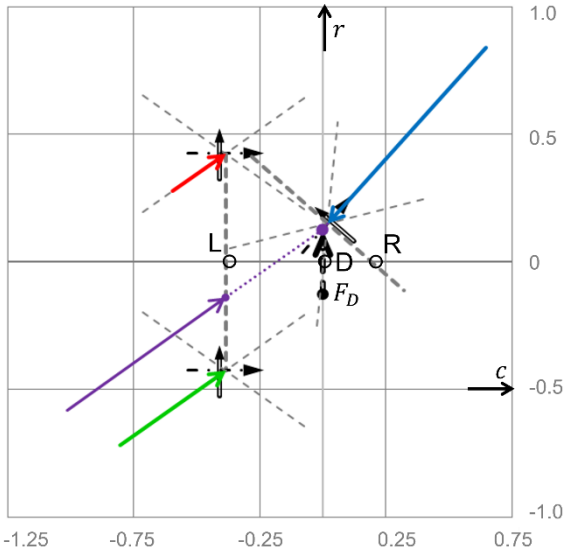

Fig. 19b: Shape-case 90L, mid-cycle, μ = 0.7, effective mid-cycle forces: the right force does not reach full slip

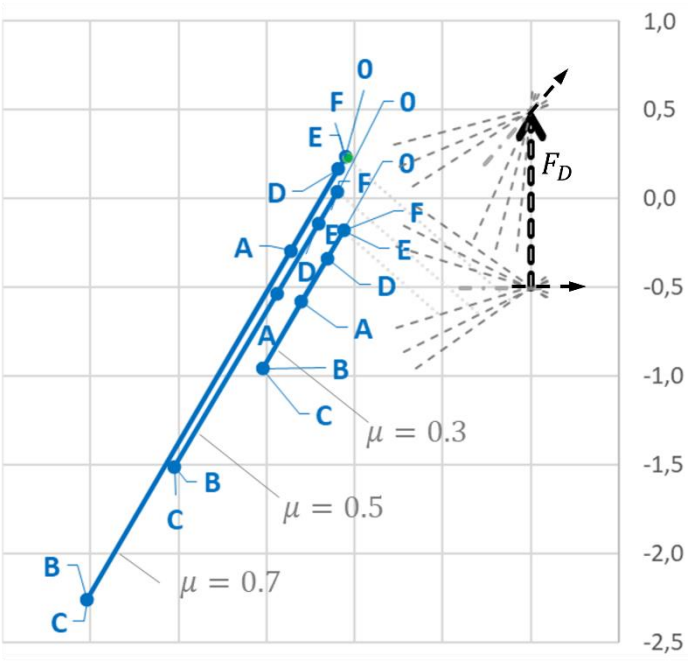

Fig. 20: Shape-case 90L, μ = 0.7, 0.5, 0.3: equilibrium tracks or normalized "force" Base-Cycles

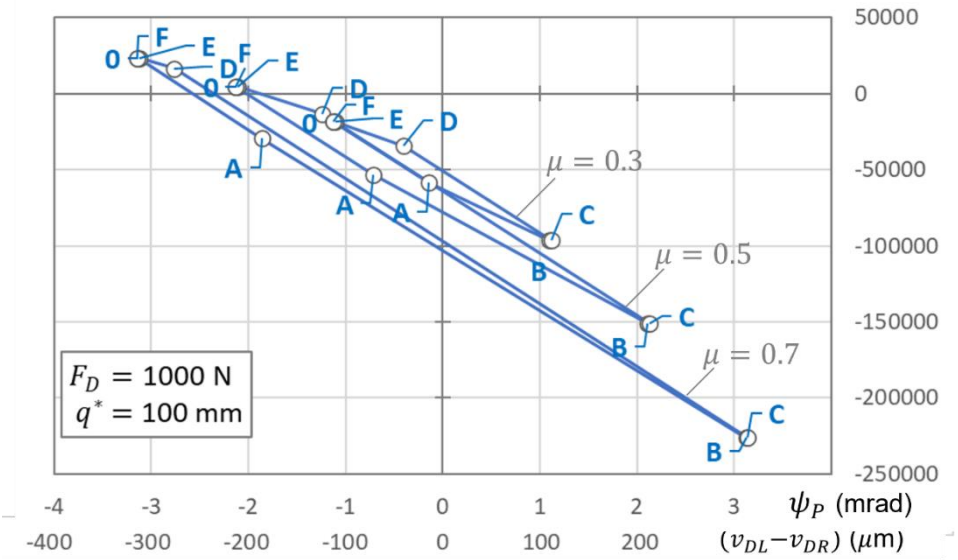

Fig. 21: Shape-case 90L, μ = 0.7, 0.5, 0.3: "moment Base-Cycle": moment M_P on platform vs. platforms relative vertical displacement $(v_{DL} - v_{DR})$ and, by way of example, platform rotation angle ψ_P for q^*=100 mm

Table 5: Shape-case 90L Transitions Chart: stick or slip condition at contacts in cycle tracts

	μ = 0.7		μ = 0.5		μ = 0.3	
tract	**in stick**	**in slip**	**in stick**	**in slip**	**in stick**	**in slip**
0-A	R_1 L_1 L_2		R_1 L_1 L_2		R_1 L_1 L_2	
A-B-C	R_1 L_1	L_2	R_1 L_1	L_2	R_1 L_1	L_2
C-D	R_1 L_1 L_2		R_1 L_1 L_2		R_1 L_1 L_2	
D-E-F	R_1 L_1	L_2	R_1 L_1	L_2	R_1 L_1	L_2

Special features

As seen in Table 5, this case exhibits two special behaviors, consequence of the missing stick-slip transition of force in R_1.

The first occurs at the end of the A-B tract, when the forces in L_1 and L_2 reach the limiting angle. Any further rotation of the platform cannot change this equilibrium, since the left contact force slips without changing value, so the right contact force, in R_1, also remains fixed and does not reach full slip, see Fig. 19b. Tract B-C, retained to preserve the cycle pattern in 3 forward tract, is not activated and corresponds to a zero platform rotation angle.

The second occurs in the same way when the return half-cycle is covered in two tracts, as already at the end of tract D-E all contact forces reach the limit angle. Tract E-F, retained to preserve the 3 backward tracts pattern, again is not activated and corresponds to a zero angle of platform rotation.

7 The Shape-Case 74L

Table 6 shows the values of distances of the left resultant force from the contacts L_1 and L_2. The choice of $b_R/h = 1.6$ determines, for $\mu = 0.7$, the % distances in the first row of Table 6.

Table 6: Shape-case 74L, distances in % of $\overline{L_1\text{-}L_2}$

Friction coeff. μ	dist. from L_1	dist. from L_2
0.7*°	0.9%	2.9%
0.5*	6.1%	30.5%
0.3*	15.1%	49.5%

* $b_R/h = 0.16$, ° $2b_L/h = 0.85$

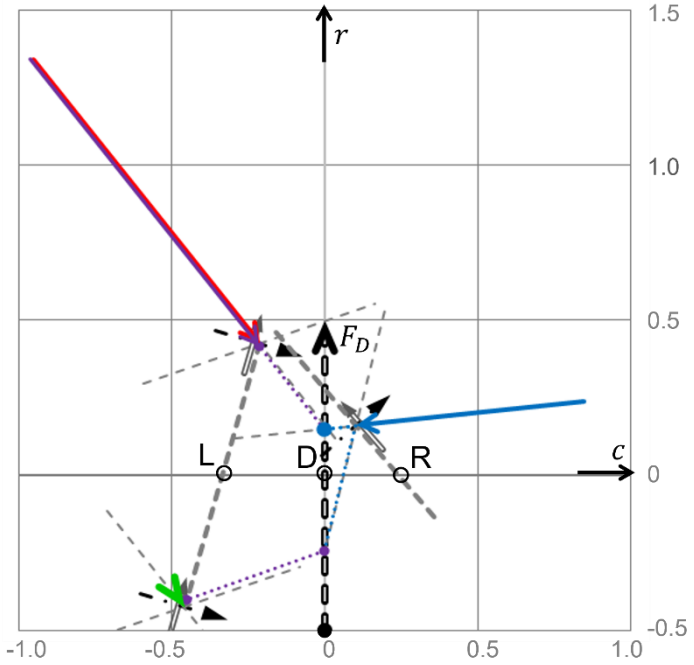

Fig. 22: Shape-case 74L, cycle-start, μ = 0.7, force lines of action at start (up) and at mid-cycle (down)

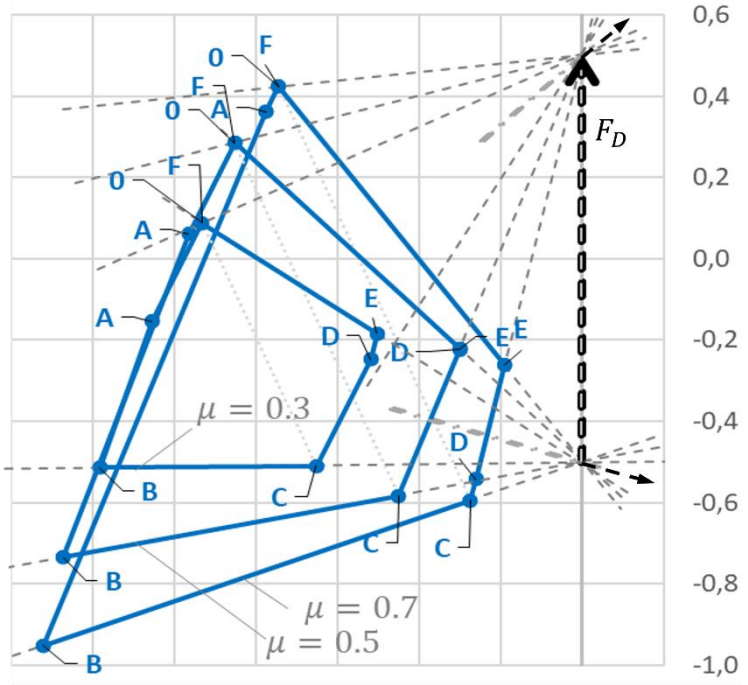

Fig. 23: Shape-case 74L, μ = 0.7, 0.5, 0.3: equilibrium tracks or normalized "force" Base-Cycles

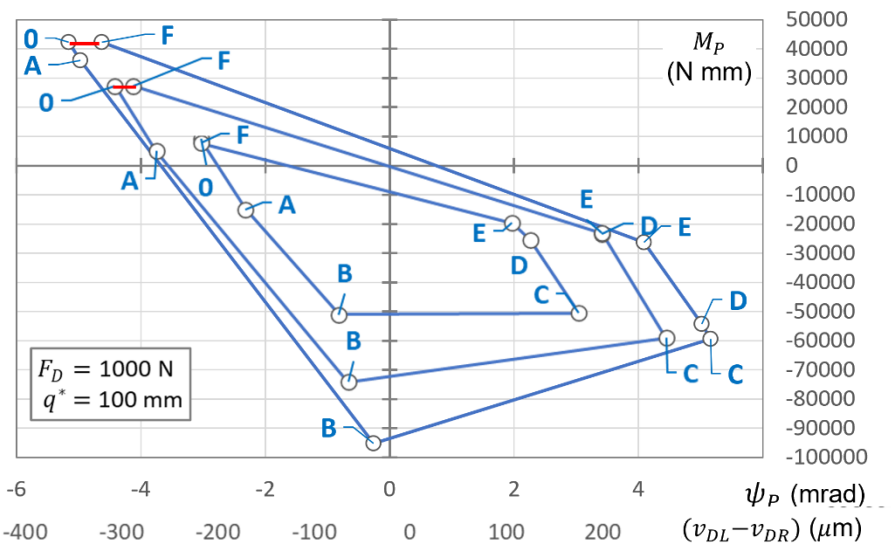

Fig. 24: Shape-case 74L, μ = 0.7, 0.5, 0.3: "moment Base-Cycle": moment M_P on platform vs. platforms relative vertical displacement $(v_{DL} - v_{DR})$ and, by way of example, platform rotation angle ψ_P for q^*=100 mm

Table 7: Shape-case 74L Transitions Chart: stick or slip condition at contacts in cycle tracts

	μ = 0.7***		μ = 0.5***		μ = 0.3	
tract	**in stick**	**in slip**	**in stick**	**in slip**	**in stick**	**in slip**
0-A	R_1 L_1 L_2		R_1 L_1 L_2		R_1 L_1 L_2	
A-B	R_1 L_1	L_2	R_1 L_1	L_2	R_1 L_1	L_2
B-C	R_1	L_1 L_2	R_1	L_1 L_2	R_1	L_1 L_2
C-D	L_1 L_2	R_1**	L_1 L_2	R_1**	L_1 L_2	R_1**
D-E	L_2	R_1** L_1	R_1 L_1	L_2	R_1 L_1	L_2
E-F	R_1	L_1 L_2	R_1	L_1 L_2	R_1	L_1 L_2

** back-slide spring release, example in Appendix 1

*** for μ = 0.7 and 0.5 full slip is reached before completion of the backward cycle

Comparing rows **B-C** and **E-F** of Table 7 with Fig. 23 one can check that tracts **B-C** and **E-F** are effectively on the left friction angle, as contacts L_1 and L_2 are in slip.

Special features

In Table 7 the symbol in red italics with double asterisk, *R1***, indicates that if during its tract, **C-D** or **D-E** in the reverse half cycle, the contact is set in "stick", as expected, and the tangential spring releases reducing the tangential force component, in this case the normal component decreases more than proportionally. The effect is to move the resultant contact force outside the limit friction angle. To avoid this, it is necessary to keep the contact in the "slide" mode along the whole tract.

For μ = 0.3 the cycle closes, i.e. **F≡0**, at the end of the succession of tracts. For μ = 0.7 and 0.5 point **F**, identified with full slip at all contacts, is reached prematurely, as seen in Fig. 24. Then, the cycle closing requires one more tract, a tract F-0 having all contacts in slip and all contact forces at constant value.

8 The Shape-Case 74R

Table 8 shows the values of distances of the left resultant force from the contacts L_1 and L_2. The choice of $b_R/h = 0.8$ determines, for $\mu = 0.7$, the distances in the first row of the table.

Table 8: Shape-case 74R, distances in % of $\overline{L_1\text{-}L_2}$

Friction coeff. μ	dist. from L_1	dist. from L_2
0.7*	17.8%	17.4%
0.5*	21.0%	34.9%
0.3*	29.8%	40.2%

* $b_R/h = 0.08$

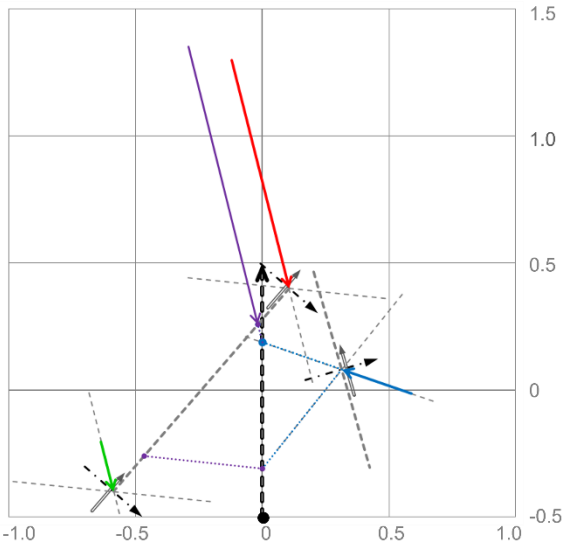

Fig. 25: Shape-case 74R, cycle-start, μ = 0.7, force lines of action at start (up) and at mid-cycle (down)

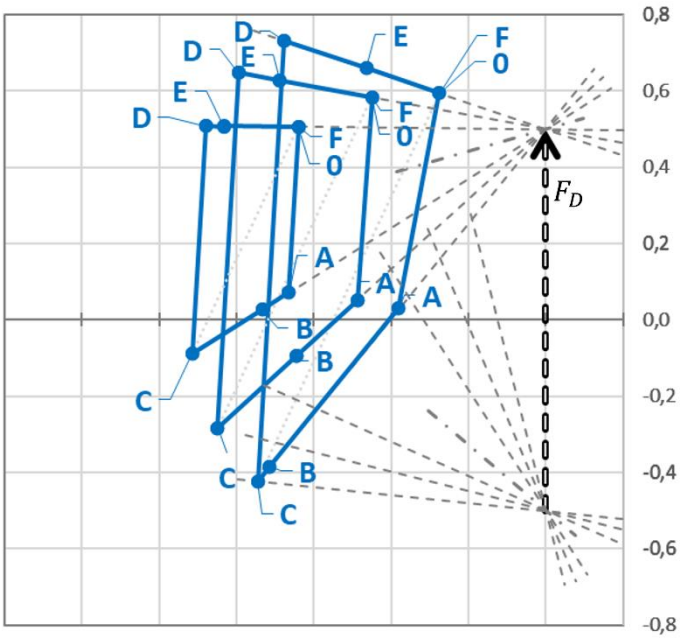

Fig. 26: Shape-case 74R, μ = 0.7, 0.5, 0.3: equilibrium tracks or normalized "force" Base-Cycle

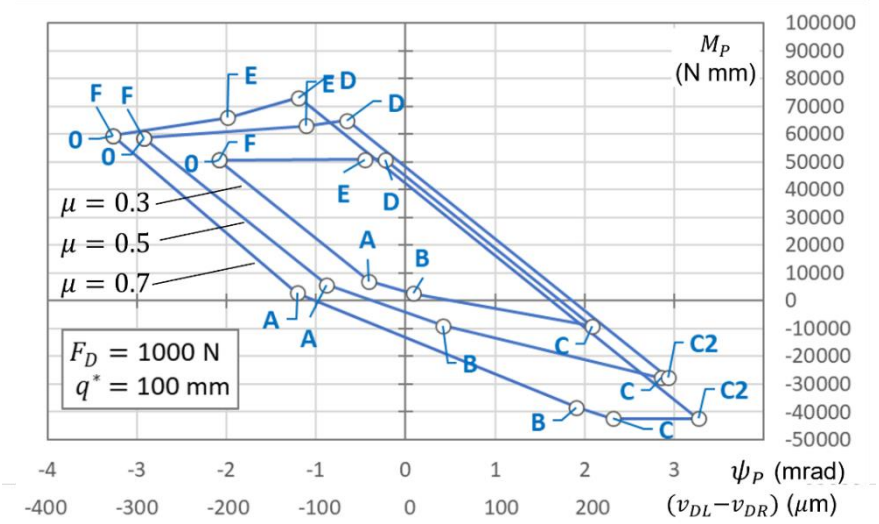

Fig. 27: Shape-case 74R, μ = 0.7, 0.5, 0.3: "moment Base-Cycle"

Table 8: Shape-case 74R Transitions Chart: stick or slip condition at contacts in cycle tracts

	μ = 0.7*		μ = 0.5*		μ = 0.3	
tract	**in stick**	**in slip**	**in stick**	**in slip**	**in stick**	**in slip**
0-A	R_1 L_2	L_1**	R_1 L_2	L_1**	R_1 L_1 L_2	
A-B	L_1 L_2	R_1	L_1 L_2	R_1	R_1 L_1	L_2
B-C	L_1	R_1 L_2	L_1	R_1 L_2	R_1	L_1 L_2
C-C$_2$		R_1 L_1 L_2		R_1 L_1 L_2	/	/
C$_2$-D**	R_1 L_1 L_2		R_1 L_1 L_2		R_1 L_1 L_2	
D-E	L_1 L_2	R_1	L_1 L_2	R_1	R_1 L_1	L_2
E-F*	L_1	R_1 L_2	L_1	R_1 L_2	R_1	L_1 L_2

* μ = 0.7, 0.5 : convergence in two iterations, the second is represented
** back-slide spring release, example in Appendix 1
*** additional tract in full slip, only for μ = 0.7 , 0.5

Special features

For μ = 0.7 and 0.5 the cycle stabilizes after two iterations.

In Table 8 the symbol in red italics with double asterisk, for *L1***, indicates that if during its tract **0-A**, the contact is set in "stick", as expected, and the tangential spring releases reducing the tangential force component, in this case the normal component decreases more than proportionally. The effect is to move the resultant contact force outside the limit friction angle. To avoid this, it is necessary to keep the contact in the "slide" mode along the whole tract.

Similar to the 74L case, where it was necessary to extend the cycle for a stretch at constant contact forces in full slip from point F to point 0 at the end of the cycle, in this 74R it is necessary to split point C at mid-cycle by reaching an auxiliary point C_2 in full slip, so that at the end of the cycle point F coincides with the initial point 0. This is necessary for μ = 0.7 and, to a much lesser extent, for μ = 0.5, and implies seven tracts instead of six. The cycle for μ = 0.3 closes with the "normal" six tracts.

9 The Shape-Case 90R

Table 9 shows the values of distances of the left resultant force from the contacts L1 and L2. The choice of $b_R/h = 0.0$ determines, for $\mu = 0.7$, the distances in the first row of the table.

Table 9: Shape-case 90R, distances in % of $\overline{L_1\text{-}L_2}$

Friction coeff. μ	dist. from L_1	dist. from L_2
0.7	28.1%	28.6%
0.5	28.6%	40.5%
0.3	31.0%	50.5%

* $b_R/h = 0.0$

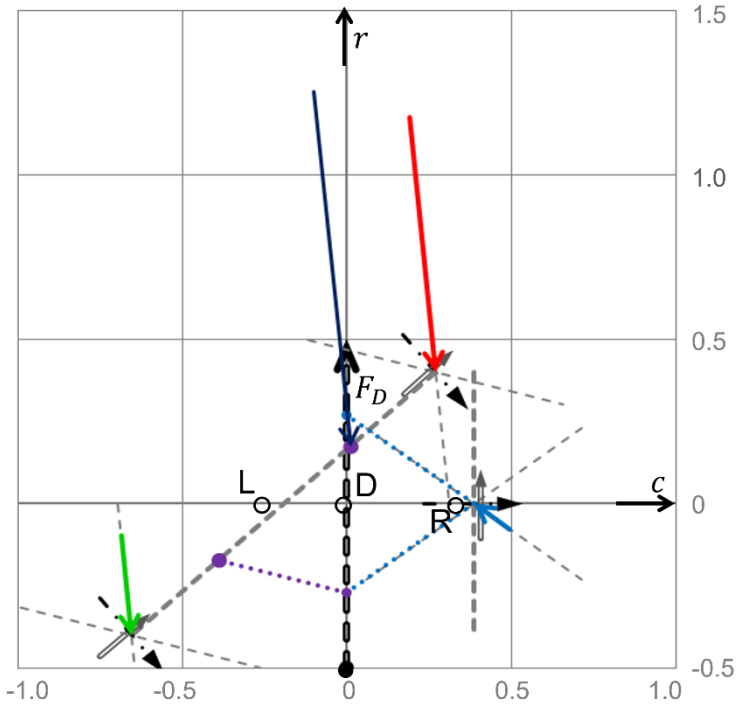

Fig. 28: Shape-case 90R, cycle-start, μ = 0.7, force lines of action at start (up) and at mid-cycle (down)

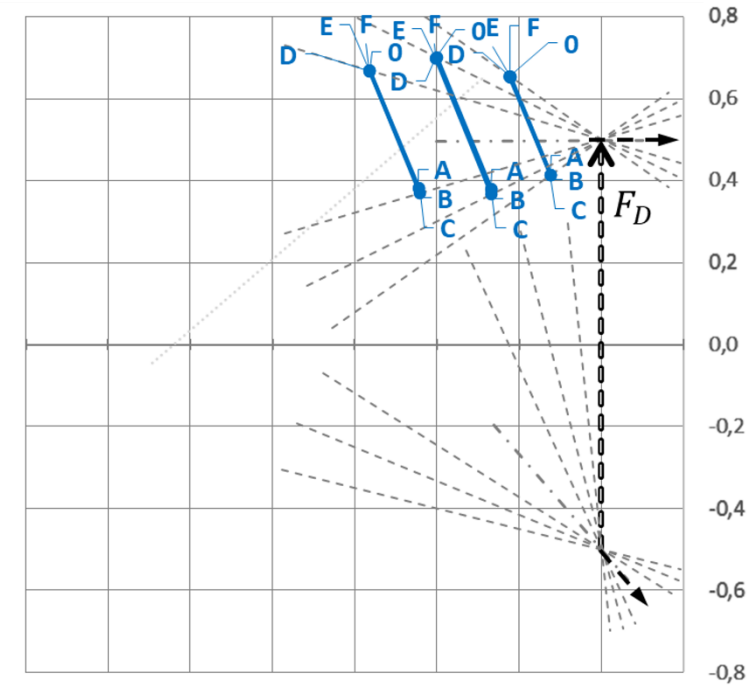

Fig. 29: Shape-case 90R, μ = 0.7, 0.5, 0.3: equilibrium tracks or normalized "force Base-Cycle"

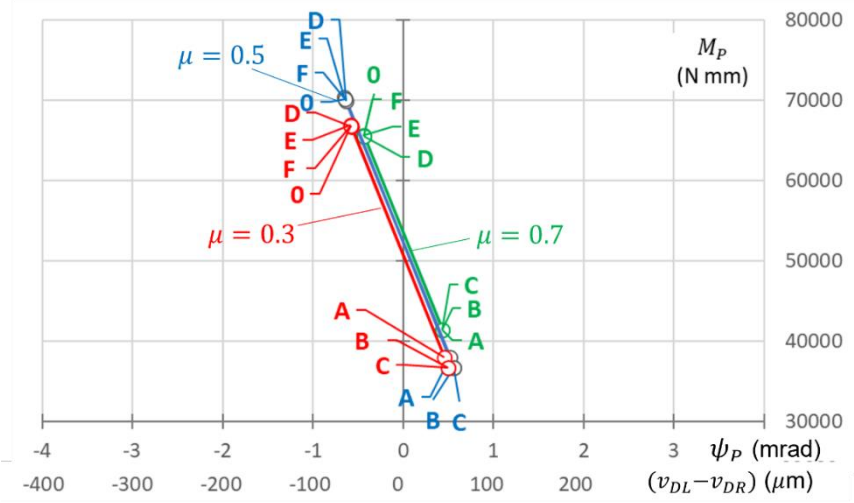

Fig. 30: Shape-case 90R, μ = 0.7, 0.5, 0.3: "moment Base-Cycle"

Table 10: Shape-case 90R Transitions Chart: stick or slip condition at contacts in cycle tracts

	μ = 0.7*		μ = 0.5*		μ = 0.3*	
tract	**in stick**	**in slip**	**in stick**	**in slip**	**in stick**	**in slip**
0-A	R_1 L_1 L_2		R_1 L_2	*L_1***	R_1 L_1 L_2	
A-B	R_1 L_2	*L_1***	R_1 L_2	*L_1***	R_1 L_2	*L_1***
B-C	L_2	R_1 *L_1***	L_2	R_1 *L_1***	R_1 L_2	*L_1***
C-D	R_1 L_1 L_2		R_1 L_1 L_2		R_1 L_1 L_2	
D-E	R_1 L_1	L_2	R_1 L_1	L_2	R_1 L_1	L_2
E-F***	L_1	R_1 L_2	L_1	R_1 L_2	L_1	R_1 L_2

* all converge in two iterations, the second is represented
** back-slide spring release, as in Appendix 1

Special features

In Table 10 the symbol in red italics with double asterisk, for *L1***, indicates that during the tract this contact cannot be set in "stick", as expected, because the normal force component decreases more than proportionally the tangential

spring releases reducing the tangential force component, in this case. The effect is to move the resultant contact force outside the limit friction angle. To avoid this, it is necessary to keep the contact in the "slide" mode along the whole tract.

10 Comparison of Shape Efficiencies

Complex stiffness components (k_{Re} , k_{Im}) are represented for all the shape-cases of Fig. 18 in Appendix B, subSections from B.1 to B.5 that show the curves in the range 0< $\psi_{P,a}$ < 20 mrad, together with their companion Tables of parameters of full stick and Base-Cycle.

Appendix B collects, for each shape, also a Table "full-sliding energy dissipation indicators" that shows the work shape factors, defined in Appendix C, that represent the amount of dissipated energy at the three contacts.

10.1 – Comparative synthesis

Data of concluding interest from the Tables of Appendix B are summarized in Table 11, for the $\mu = 0.3$ and $\mu = 0.5$ only, however not for $\mu = 0.7$, a friction angle that was considered to ensure regular working without liftoff throughout the whole possible friction range, hence the corresponding choice of b_R/h. The following values are commented through scores:

- $\psi_{P,a,fs}$: platform angle at the end of full-slip, not evaluated, variability limited
- $k_{Re,init}$: initial stiffness, best ❶ if value is highest
- $\psi_{P,a,BC}$: platform angle at Base-Cycle, best ❶ if value is lowest
- $k_{Re,BC}$: real stiffness component at Base-Cycle, best ❶ if value is highest
- $k_{Im,BC}$: imaginary stiffness component at Base-Cycle, not evaluated
- w_M : work shape factor for platform moment: best ❶ if value is highest

Case 90L collects the highest number of positive evaluations, case 74L the highest number of negative ones.

Case 90R has the critical defect of a lowest w_M , i.e., the lowest damping capability in the event of full slip. Moreover, sliding takes place only on the single contact pad in R1, Tab. B5.2, while, on the contrary, case 90L shares dissipation work on pads in L1 and L2 in a quite balanced manner, Tab. B1.2.

A curious result holds for case 60sym, Tab.B3.2 dissipation on contact R1 is always 50% of the total the rest is shared by about two thirds on L1 and one third on L2, independently of the friction coefficient. This proportion holds as well for L1 and L2 in case 90L with $\mu = 0.3$, where, however, these two contacts dissipate the whole amount of energy.

Table 11: Principal performance indicators of dampers of the 60sym family, and scores according to friction and shape: ❶ best choice, ❷ second best, ⑤ worst

		90L	74L	60sym	74R	90R
$\mu = 0.3$	$\psi_{P,a,fs}$	0,49	0,36	0,53	0,84	0,52
	$k_{Re,init}$	❶ 40851	33549	28741	25849	27805
	$\psi_{P,a,BC}$	❷ 1,12	⑤ 3,05	1,50	2,09	❶ 0,54
	$k_{Re,BC}$	❶ 35244	⑤ 8331	21634	14245	❷ 27676
	$k_{Im,BC}$	4490	6513	5057	7168	168
	w_M	❶ 0,780	0,596	❷ 0,636	0,596	⑤ 0,299
$\mu = 0.5$	$\psi_{P,a,fs}$	0,71	0,33	0,67	1,02	0,58
	$k_{Re,init}$	❶ 40851	33549	28741	25983	27805
	$\psi_{P,a,BC}$	❷ 2,13	⑤ 4,43	2,18	2,94	❶ 0,61
	$k_{Re,BC}$	❶ 37078	⑤ 8672	21634	14908	❷ 27779
	$k_{Im,BC}$	3185	6957	4921	7020	33
	w_M	❶ 1,552	0,866	❷ 0,924	0,866	⑤ 0,337

Attention is drawn to the fact that both in the case pair 90L and 90R, as well as in the case pair 74L and 74R, the two members of the pair have markedly different results. This is because on the same geometric shape, simply flipped horizontally, the two contacts representing the flat surface and the single contact on the opposite side always remain on the left or right respectively. This completely changes the shape of the "equilibrium tracks". An additional cause of

difference is due to the different choice of the position of the single contact R1 to “center” the resultant on the flat contact in the case of maximum coefficient of friction. These differences would not exist if the same shapes were used with perfectly ideal plane contacts, evenly distributed on both surfaces, as in the case of ideal wedge dampers.

As has been demonstrated experimentally [24], the inevitable machining imperfections on the flat contact surfaces of a Siemens-type damper result in erratic behaviour due to the lack of precise control over the position of the contacts. It is relatively straightforward to envisage the potential consequences of the aforementioned issues in a real-world context, as opposed to idealised numerical models. This is particularly pertinent in the case of a wedge damper, where the challenge of machining imperfections (as duly acknowledged in reference [12]) is compounded by the possibility of misalignment between adjacent blade platforms (which, it must be noted, does not appear to be a primary focus within the extant literature). In contrast to the contact-asymmetric contact damper [16], the wedge damper is unable to adapt to such circumstances.

11 Conclusions

The algorithm developed in a previous paper for direct calculation of the hysteresis “Base-Cycle” of contact-asymmetric UDs was here used as a method of comparing the effectiveness of damper shapes. Scaling according to either damper or platform size was the subject of the previous paper, and can be applied separately.

It was discussed how to adjust the position of the single contact on its damper side to avoid liftoff when the damper-platform friction coefficient is highest, at 0.7, a value at cold start. The hysteresis cycles for rotations of blade platforms during In-Phase vibrations equal to - and higher than – that of the Base-Cycle were then examined for friction coefficients 0.5 and 0.3, i.e. at the limits of the range expected in operating conditions at temperature. On this basis, the isosceles 45°/45° damper was examined, concluding that at the highest operational friction coefficient 0.5 it would work in marginal conditions not guaranteeing absence of liftoff.

For this reason, the method was applied to a family of dampers with a smaller vertex angle. This family is composed of five dampers obtained by distortion of an isosceles of 60° aperture at the vertex. The five study cases include two dampers with 90° inclination of either the left or the right side, named 90L and 90R, and two intermediate dampers having the left or the right side inclines by 74°, named 74L and 74R. In all cases the left surface accommodates a couple of contact pads, while the right surface contains the single contact.

For each of the five dampers, and for the three friction coefficients, the different problems were examined that arise in calculating the hysteresis cycle at the onset of the total full-slip, called Base-Cycle, described first in a “force” form, otherwise named “equilibrium track diagram”, then as a platform “moment” diagram. Moreover, for each damper a Transitions Chart is given, that serves to elucidate the variety of special problems that are encountered in calculating the fundamental “equilibrium track” diagram.Shapes for both types of Base-Cycles are provided for the whole damper family and the three friction coefficients, thus covering a variety of cases that give a deep insight into the damper behavior.

Applying the “moment Base-Cycle” concept to the Platform Centered Reduction technique, the dampers of the studied family are described by their characteristic diagrams of the real and imaginary components of the complex stiffness on the platform rotation.

Finally, the values of the dissipated energies at the damper contact pads are determined, the sum of which is checked against the total energy dissipated by the moment of contact forces acting on the platform, consistent with Platform Centered Reduction.

References

[1] R. E. Kielb, J. H. Griffin, C. H. Menq. Evaluation of a Turbine Blade Damper Using an Integral Approach. Structures, Structural Dynamics and Materials Conference, Williamsburg, VA, US, 1988. https://doi.org/10.2514/6.1988-2400

[2] J.H. Griffin. Friction Damping of Resonant Stresses on Gas Turbine Engine Airfoils. J. Eng. Power. 102(2): 329-333, 1980. https://doi.org/10.1115/1.3230256

[3] J. H. Griffin. A Review of Friction Damping of Turbine Blade Vibration. International Journal of Turbo and Jet Engines, 7. 297-307, 1990. https://doi.org/10.1515/TJJ.1990.7.3-4.297

[4] B. D. Yang and C. H. Menq. Characterization of Contact Kinematics and Application to the Design of Wedge Dampers in Turbomachinery Blading, Part I: Stick-slip Contact Kinematics. ASME J. of Eng. for Gas Turbines and Power, Vol. 120, No.2, 410-417, 1998. https://doi.org/10.1115/1.2818138 ; Part 2—Prediction of Forced Response and Experimental Verification, Vol. 120, No.2, 418-423, 1998. https://doi.org/10.1115/1.2818139

[5] K. Y. Sanliturk, D. J. Ewins and A.B. Stanbridge. Under-platform Dampers for Turbine Blades: Theoretical

Modelling, Analysis and Comparison with Experimental Data, ASME J. Eng. for Gas Turbines and Power, Vol. 123, 919-929, 2001. https://doi.org/10.1115/1.1385830

[6] L. Panning, K. Popp, W. Sextro, F. Goetting, A. Kayser and I. Wolter. Asymmetrical underplatform dampers in gas turbine bladings: Theory and Application. Proc. of ASME Turbo Expo, Vienna, 2004. https://doi.org/10.1115/GT2004-53316

[7] E. V. Petrov. Explicit Finite Element Models of Friction Dampers in Forced Response Analysis of Bladed Disks, Journal of Engineering for Gas Turbines and Power. Vol. 130 / 022502-1, 2008. https://doi.org/10.1115/1.2772633

[8] J. Szwedowicz. Structural Design of Aircraft Engines, Chapter 9: Bladed Disks: Non-Linear Dynamics. NATO-OTAN STO Educational Notes: RTO-EN-AVT-207, 2012. https://www.sto.nato.int/publications/STO%20Educational%20Notes/Forms/Document%20Set%20View.aspx

[9] M. Krack, S. Tatzko, L. Panning-von Scheidt and J. Wallaschek. Reliability optimization of friction-damped systems using nonlinear modes. Journal of Sound and Vibration. 333, 2699–2712, 2014. https://doi.org/10.1016/j.jsv.2014.02.008

[10] M. M. Gola, T. Liu. A direct experimental–numerical method for investigations of a laboratory under-platform damper behavior. Int. J. Solids Struct. 51 (25), 4245–4259, 2014. https://doi.org/10.1016/j.ijsolstr.2014.08.011

[11] M. Krack , L. Salles and F. Thouverez. Vibration Prediction of Bladed Disks Coupled by Friction Joints. Arch. Comput. Methods Eng. 24, 589–636, 2017. https://doi.org/10.1007/s11831-016-9183-2

[12] L. Pesaresi, L. Salles, A. Jones, J. S. Green and C. W. Schwingshackl. Modelling the nonlinear behaviour of an underplatform damper test-rig for turbine applications. Mech. Sys. Signal Proc. 85, 662–679, 2017. https://doi.org/10.1016/j.ymssp.2016.09.007

[13] M. Hüls, L. Panning-von Scheidt and J. Wallaschek. Influence of Geometric Design Parameters onto Vibratory Response and High-Cycle Fatigue Safety for Turbine Blades with Friction Damper, J. Eng. Gas Turbines Power., 141(4): 041022, 2019. https://doi.org/10.1115/1.4040732

[14] Y. Yuan, A. Jones, R. Setchfield and C. Schwingshackl. Robust design optimisation of underplatform dampers for turbine applications using a surrogate model. J Sound Vib. 494(6):115528, 2020. https://doi.org/10.1016/j.jsv.2020.115528

[15] S. M. Pourkiaee, S. Zucca and R. G. Parker, Relative cyclic component mode synthesis: A reduced order modeling approach for mistuned bladed disks with friction interfaces. Mechanical Systems and Signal Processing, Volume 163, 108197, ISSN 0888-3270, 2022. https://doi.org/10.1016/j.ymssp.2021.108197, routines in https://www.knowledge-share.eu/en/patents/nova-nonlinear-vibrations-of-assemblies

[16] M. M. Gola. A general geometrical theory of turbine blade underplatform asymmetric dampers. Mechanical Systems and Signal Processing, Vol. 191,110167, 2023. https://doi.org/10.1016/j.ymssp.2023.110167

[17] T. M. Cameron, J. H. Griffin, R. E. Kielb and T. M. Hoosac. An Integrated Approach for Friction Damper Design. ASME. J. Vib. Acoust. 112 (2),175–182, 1990. https://doi.org/10.1115/1.2930110

[18] M. Bobo. Vibration damping of gas turbine engine buckets, United States Patent N. 5,156,528. Inventor Melvin Bobo, General Electric, 1992

[19] C. Gastaldi and M. M. Gola. A random sampling strategy for tuning contact parameters of underplatform dampers. GT2015-42834, Proc. ASME Turbo Expo, TE2015, 2015. https://doi.org/10.1115/GT2015-42834

[20] C. W. Schwingshackl, E. P. Petrov and D. Ewins. Measured and estimated friction interface parameters in a nonlinear dynamic analysis. Mechanical Systems and Signal Processing, Vol. 28, 574-584, 2012. https://doi.org/10.1016/j.ymssp.2011.10.005

[21] S. Filippi, A. Akay and M. M. Gola. Measurement of Tangential Contact Hysteresis During Microslip. ASME Journal of Tribology, v. 126-3, pp. 482-489, 2004. https://doi.org/10.1115/1.1692030

[22] D. Li, C. Xu, T. Liu, M. M. Gola M.M and L. Wen. A modified IWAN model for micro-slip in the context of dampers for turbine blade dynamics. Mechanical Systems and Signal Processing, online 2018.11.17, Vol. 121, 14-30, 2019. https://doi.org/10.1016/j.ymssp.2018.11.002

[23] C. Gastaldi and M. M. Gola. Estimation accuracy vs. engineering significance of contact parameters for solid dampers. Journal of the Global Power and Propulsion Society,1:71-83, 2017. https://doi.org/10.22261/VLXC9F

[24] C. Gastaldi, T. Berruti T and M. M. Gola. The Effect of Surface Finish on the Proper Functioning of Underplatform Dampers. J. Vib. Acoust. 142(5): 051103, 2020. https://doi.org/10.1115/1.4046954

[25] D. Zhang, B. Gao, J. Hong, J. Fu, X. Ge. Experimental investigation on dynamic response of flat blades with underplatform dampers. Chinese Journal of Aeronautics, Volume 32, Issue 12, 2667-2678, 2019. https://doi.org/10.1016/j.cja.2019.04.022

[26] S. Hu, H. She, G. Yang, C. Zang, C. Li. The Influence of Interface Roughness on the Vibration Reduction Characteristics of an Under-Platform Damper. Appl. Sci.13 (2023) 2128. https://doi.org/10.3390/app13042128

[27] C. Gastaldi and M. M. Gola. Platform Centered Reduction: A Process Capturing the Essentials for Blade-Damper Coupled Optimisation. ASME Journal of Engineering for Gas Turbines and Power, 143(8), 081001, 2021. https://doi.org/10.1115/1.4049187
[28] C. Gastaldi and M. M. Gola. Non-Linear Damper-Blade Coupling Calculations Reduced to Essentials, J. Eng. Gas Turbines Power., 145(2): 021016, 2023. https://doi.org/10.1115/1.4055414
[29] C. Gastaldi and M. M. Gola. Convergence-free mapping of non-linear damper-blade performance. Mechanical Systems and Signal Processing 208, 111062, 2024. https://doi.org/10.1016/j.ymssp.2023.111062
[30] D. Botto, C. Gastaldi, M. M. Gola and M. Umer. An experimental investigation of the dynamics of a blade with two under-platform dampers. J. Eng. Gas Turbines Power 140 (3), 2018. https://doi.org/10.1115/1.4037865 032504
[31] C. Gastaldi, J. Gross, M. Scheel, T. M. Berruti and M. Krack. Modeling complex contact conditions and their effect on blade dynamics. J. Eng. Gas Turbines Power 143 (1), 2021. https://doi.org/10.1115/1.4049186
[32] E. Ferhatoglu, S. Zucca. On the non-uniqueness of friction forces and the systematic computation of dynamic response boundaries for turbine bladed disks with contacts, Mechanical Systems and Signal Processing, Volume 160, 107917, ISSN 0888-3270, 2021. https://doi.org/10.1016/j.ymssp.2021.107917

Appendix

A The Back-Slide Spring Release

At any of the contacts, L1 or L2 or R1, is represented in Fig. A.1 a), where the contact surface D of the damper slides relative to the platform P until the onset of sliding is reached, i.e., $T = \mu N$. The normal contact force N on damper is due to compression of the normal spring k_n and the tangential force T is due to the elongation t_{DP} of the tangential spring k_t.

Fig. A.1 b) shows a backward damper-to-platform motion Δt_{DP}, a tangential force release ΔT and a normal compression release ΔN due to normal release Δn_{DP}, with $\Delta T < \mu\, \Delta N$ then the resultant force falling inside the friction angle. In this case the contact model is “stick”.

Fig. A.1c) represents an impossible situation when the stick model would be adopted while the normal spring release Δn^*_{DP} produces a normal force reduction ΔN^*, what would bring the resultant contact force outside the friction angle. To overcome the problem, a slip contact model must be adopted as in Fig. A.1 d), where the sliding contact condition is imposed $\Delta T = \mu\, \Delta N^*$ corresponding to let the contact back-slide by an amount Δs compatible with such tangential force variation.

For equations, please refer to [16] at “Appendix 4 – The local contact matrices”.

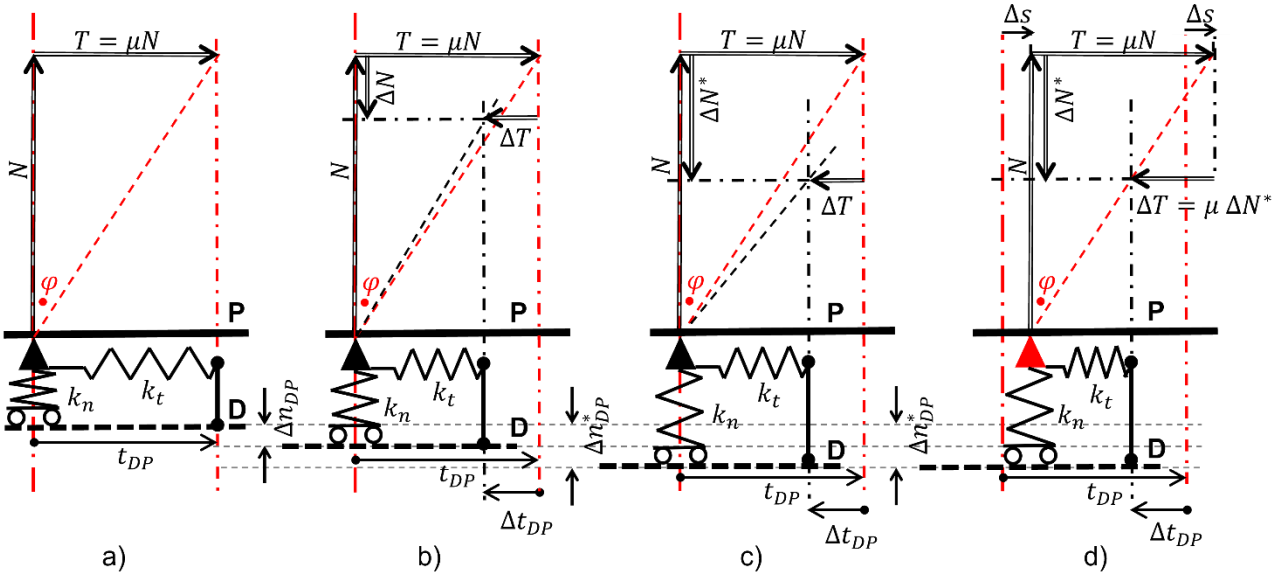

Fig. A.1: P: platform; D damper; t_{DP}: damper-to-platform tangential motion, ; a): onset of contact slip, max elongation t_{DP} of tangential spring; b) backward relative motion Δt_{DP} , spring release in stick; c) impossible stick solution; d) contact slides back by Δs , increased spring release to $\Delta T = \mu\, \Delta N^*$

Figs A.2 show by way of example the case 90L, where the tract **0-A** requires setting the contact L_1 in "back-slip" instead of "stick". Fig. A.2a shows force $F_{L1,A}$ on the limit friction angle as the initial force $F_{L1,0}$. Were the contact in L_1 set in stick, then, Fig. A.2b, the force $F_{L1,Aw}$ (w: for "wrong") would fall outside the limit friction angle. All other forces would be wrong as well.

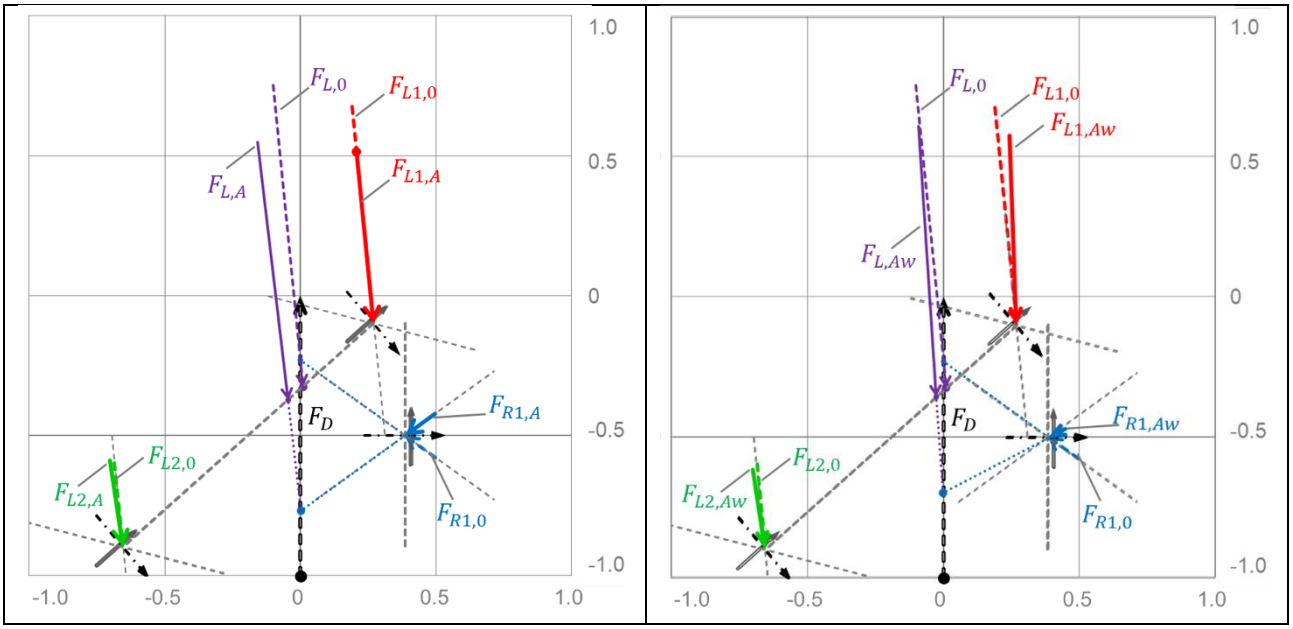

Fig. A.2: (Left) case 90L, $\mu = 0.7$, contact forces at initial point **0** and at final point **A** of the first tract **0-A**, contact in L_1 set "back-slip", R_1 and L_2 "stick". (Right) case 90L, $\mu = 0.7$, contact forces at initial point **0** and at final point **A** of the first tract **0-A**, all contacts on R_1 , L_1 , L_2 set "stick"

B Complex Stiffness Components and Energy Dissipation Indicators for the Family of Cases

Complex stiffness components (k_{Re} , k_{Im}) are represented in this Appendix for all shape-cases of Fig. 18, in subSections from B.1 to B.5 that show the curves in the range 0< $\psi_{P,a}$ < 20 mrad, together with their companion Tables of parameters of full stick and Base-Cycle.

Companion tables collect the values of:

- $\psi_{P,a,fs}$: value of $\psi_{P,a}$ at the end of full-stick
- $k_{Re,fs}$: real rotational stiffness of platform in initial full-stick
- $\psi_{P,a,BC}$: value of $\psi_{P,a}$ at Base-Cycle
- $k_{Re,BC}$: real rotational stiffness of platform at Base-Cycle
- $k_{Im,BC}$: imaginary rotational stiffness of platform at Base-Cycle

Then, for each shape, work shape factors, defined in Appendix C, are collected in a Table "full-sliding energy dissipation indicators" that represent the amount of relative dissipated energy at the three contacts. Note that the sum of the indicators of dissipated energy on the three contacts (rows 2, 3, 4) equals the corresponding value calculated in row 5 for the moment on the platform.

B.1 – Shape-case 90L

For this case $2b_L = 0.85\ h$, as explained in Section 6

Table B1.1: Parameters of full stick (fs) and Base-Cycle (BC) of Fig. B1.1

μ	$\psi_{P,a,fs}$	$k_{Re,fs}$	$\psi_{P,a,BC}$	$k_{Re,BC}$	$k_{Im,BC}$
0.7	0.64	41150*	3.14	40191	1077
0.5	0.71	40851	2.13	37078	3185
0.3	0.49	40851	1.12	35244	4490

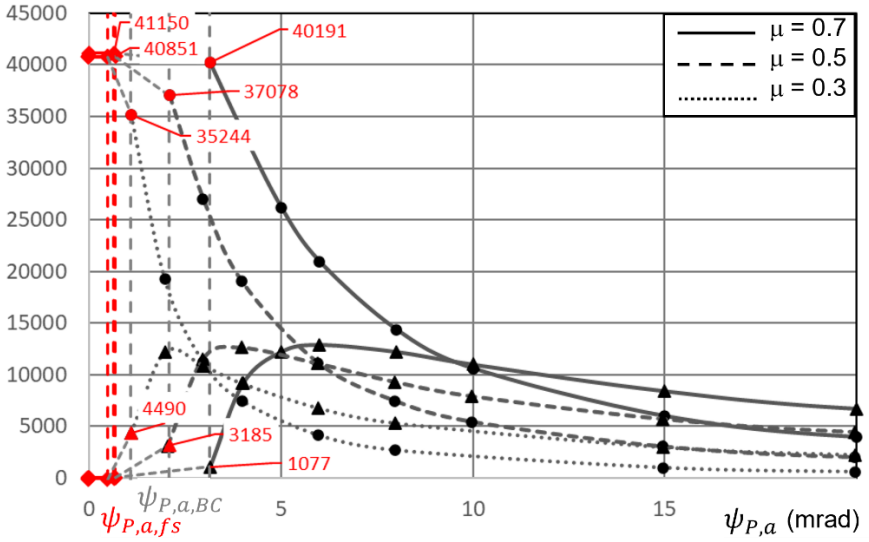

Fig. B1.1: Shape-case 90L, μ = 0.7, 0.5, 0.3: real, k_{Re} , and imaginary, k_{Im} (N mm/mrad) components of platform complex rotational stiffness vs. amplitude of alternating platform rotation $\psi_{P,a}$ (mrad)

Table B1.2: Full-slip energy dissipation of shape-case 90L

	Work shape factors	$\mu = 0.7$		$\mu = 0.5$		$\mu = 0.3$	
1	w_{R1} : work shape factor on contact R_1	0.000	0%	0.000	0%	0,000	0%
2	w_{L1} :work shape factor on contact L_1	1.317	53%	0.927	60%	0.501	64%
3	w_{L2} : work shape factor on contact L_2	1.182	47%	0.625	40%	0.279	36%
4	**Sum** $w_{R1} + w_{L1} + w_{L2}$	**2.499**	**100%**	**1.552**	**100%**	**0.780**	**100%**
5	w_M : work shape factor of moment	***2.499***	**/**	***1.552***	**/**	***0.780***	**/**

Note the percentage of the total energy dissipated on each contact. With this shape the right contact does not dissipate, then it does not wear, conforming to the fact that it always remains in stick (see Fig.19a, 19b, 20).

B.2 – Shape-case 74L

Table B2.1: Parameters of full stick (fs) and Base-Cycle (BC) of Fig. B2.1

μ	$\psi_{P,a,fs}$	$k_{Re,fs}$	$\psi_{P,a,BC}$	$k_{Re,BC}$	$k_{Im,BC}$
0.7	0.092	33788	5.159	9243	7517
0.5	0.333	33549	4.429	8672	6957
0.3	0.360	33549	3.047	8332	6513

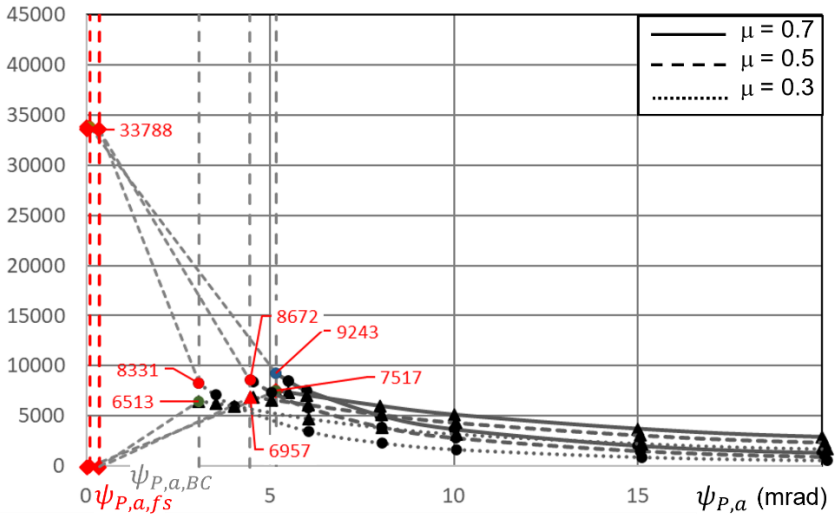

Fig. B2.1: Shape-case 74L, μ = 0.7, 0.5, 0.3: real, k_{Re} , and imaginary, k_{Im} (N mm/mrad) components of platform complex rotational stiffness vs. amplitude of alternating platform rotation $\psi_{P,a}$ (mrad)

Table B2.2: Full-slip energy dissipation of shape-case 74L

	Work shape factors	$\mu = 0.7$		$\mu = 0.5$		$\mu = 0.3$	
1	w_{R1}: work shape factor on contact R_1	0.356	35%	0.303	35%	0.209	35%
2	w_{L1} :work shape factor on contact L_1	0.530	52%	0.427	49%	0.278	47%
3	w_{L2}: work shape factor on contact L_2	0.131	13%	0.136	16%	0.109	18%
4	**Sum** $w_{R1} + w_{L1} + w_{L2}$	**1.017**	**100%**	**0.866**	**100%**	**0.596**	**100%**
5	w_M : work shape factor of moment	***1.017***	**/**	***0.866***	**/**	***0.596***	**/**

B.3 – Shape-case 60sym

Table B2.1: Parameters of full stick (fs) and Base-Cycle (BC) of Fig. B3.1

μ	$\psi_{P,a,fs}$	$k_{Re,fs}$	$\psi_{P,a,BC}$	$k_{Re,BC}$	$k_{Im,BC}$
0.7	0.60	28741	2.56	21679	4583
0.5	0.67	28741	2.18	21634	4921
0.3	0.53	28741	1.50	21634	5057

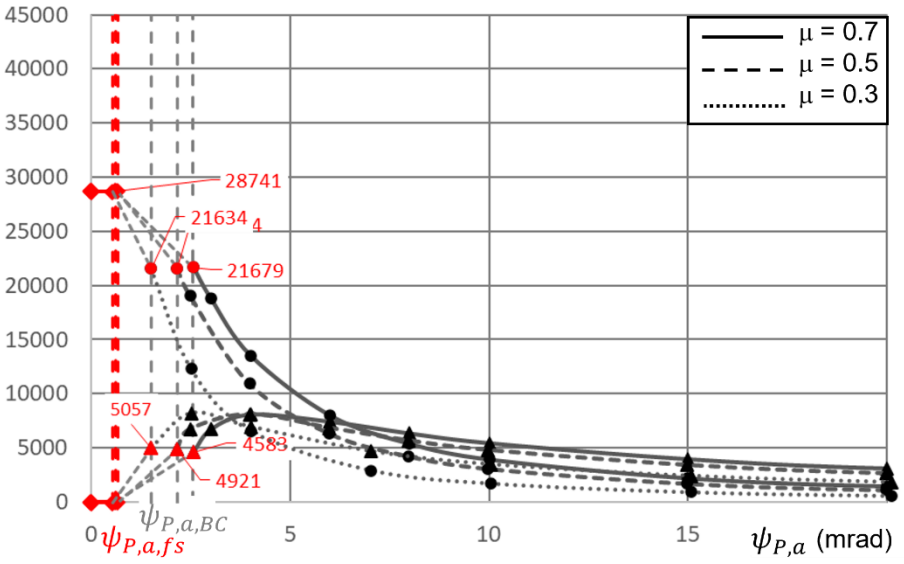

Fig. B3.1: Shape-case 60sym - μ = 0.7, 0.5, 0.3: complex stiffness components

Table B3.2: Full-slip energy dissipation of shape-case 60sym

	Work shape factors	$\mu = 0.7$		$\mu = 0.5$		$\mu = 0.3$	
1	w_{R1}: work shape factor on contact R_1	0.542	50%	0.462	50%	0.318	50%
2	w_{L1}: work shape factor on contact L_1	0.366	34%	0.312	34%	0.215	34%
3	w_{L2}: work shape factor on contact L_2	0.176	16%	0.150	16%	0.103	16%
4	**Sum** $w_{R1} + w_{L1} + w_{L2}$	**1.085**	**100%**	**0.924**	**100%**	**0.636**	**100%**
5	w_M : work shape factor of moment	***1.085***	**/**	***0.924***	**/**	***0.636***	**/**

B.4 – Shape-case 74R

Table B4.1: Parameters of full stick (fs) and Base-Cycle (BC) of Fig. B4.1

μ	$\psi_{P,a,fs}$	$k_{Re,fs}$	$\psi_{P,a,BC}$	$k_{Re,BC}$	$k_{Im,BC}$
0.7	1.030	27426	3.270	16194	7452
0.5	1.023	25983	2.935	14908	7020
0.3	0.841	25849	2.089	14245	7168

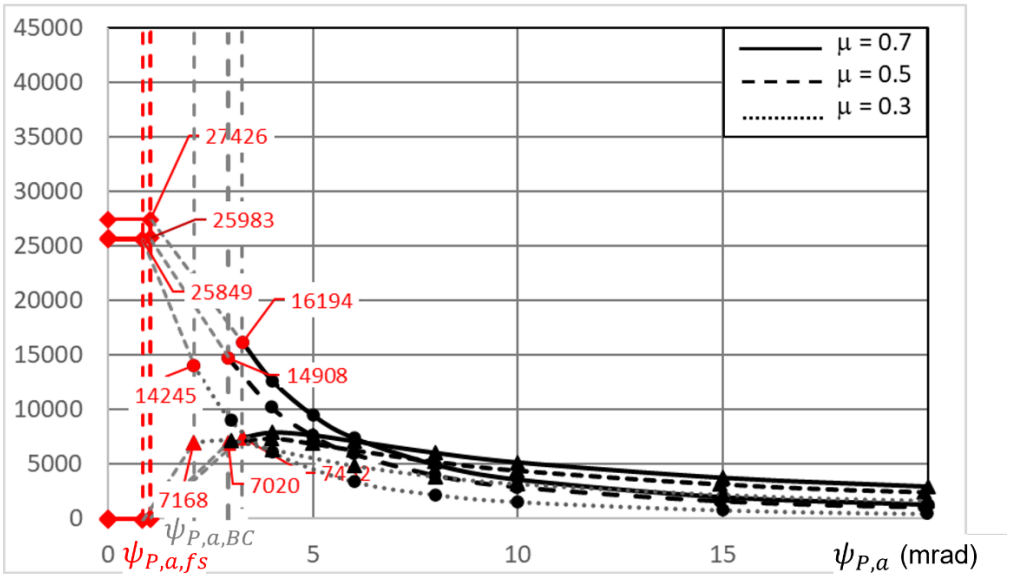

Fig. B4.1: Shape-case 74R, μ = 0.7, 0.5, 0.3: real, k_{Re} , and imaginary, k_{Im} (N mm/mrad) components of platform complex rotational stiffness vs. amplitude of alternating platform rotation $\psi_{P,a}$ (mrad)

Table B4.2: Full-slip energy dissipation of shape-case 74R

	Work shape factors	$\mu = 0.7$		$\mu = 0.5$		$\mu = 0.3$	
1	w_{R1}: work shape factor on contact R_1	0.661	65%	0.563	65%	0.387	65%
2	w_{L1}: work shape factor on contact L_1	0.201	20%	0.182	21%	0.131	22%
3	w_{L2} : work shape factor on contact L_2	0.155	15%	0.121	14%	0.078	13%
4	**Sum** $w_{R1} + w_{L1} + w_{L2}$	**1.017**	**100%**	**0.866**	**100%**	**0.596**	**100%**
5	w_M : work shape factor of moment	***1.017***	**/**	***0.866***	**/**	***0.596***	**/**

B.5 – Shape-case 90R

Table B5.1: Parameters of full stick (fs) and Base-Cycle (BC) of Fig. B5.1

μ	$\psi_{P,a,fs}$	$k_{Re,fs}$	$\psi_{P,a,BC}$	$k_{Re,BC}$	$k_{Im,BC}$
0.7	0.434	27799	0.436	27797	79
0.5	0.580	27805	0.608	27779	33
0.3	0.519	27805	0.543	27676	168

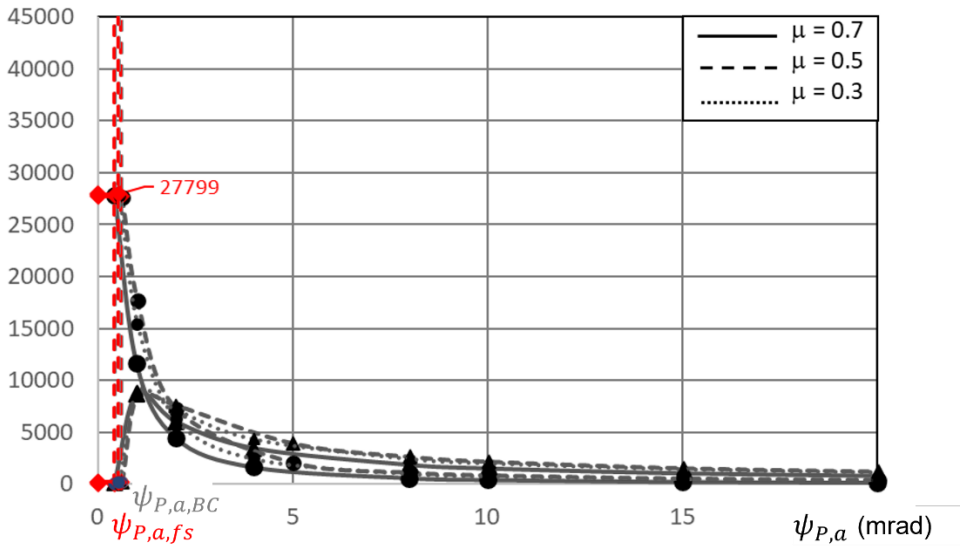

Fig. B5.1: Shape-case 90R, μ = 0.7, 0.5, 0.3: real, k_{Re} , and imaginary, k_{Im} (N mm/mrad) components of platform complex rotational stiffness vs. amplitude of alternating platform rotation $\psi_{P,a}$ (mrad)

Table B5.2: Full-slip energy dissipation of shape-case 90R

	Work shape factors	$\mu = 0.7$		$\mu = 0.5$		$\mu = 0.3$	
1	w_{R1}: work shape factor on contact R_1	0.242	100%	0.338	100%	0.301	100%
2	w_{L1}: work shape factor on contact L_1	0.000	0%	0.000	0%	0.000	0.000%
3	w_{L2}: work shape factor on contact L_2	0.000	0%	0.000	0%	0.000	0.000%
4	**Sum** $w_{R1} + w_{L1} + w_{L2}$	**0.242**	**100%**	**0.338***	**100%**	**0.301**	**100%**
5	w_M : work shape factor of moment	0.242	/	0.337*	/	0.299*	/

* differences due to cycle convergence approximation

C Definition of Work Shape Factors in Full Sliding

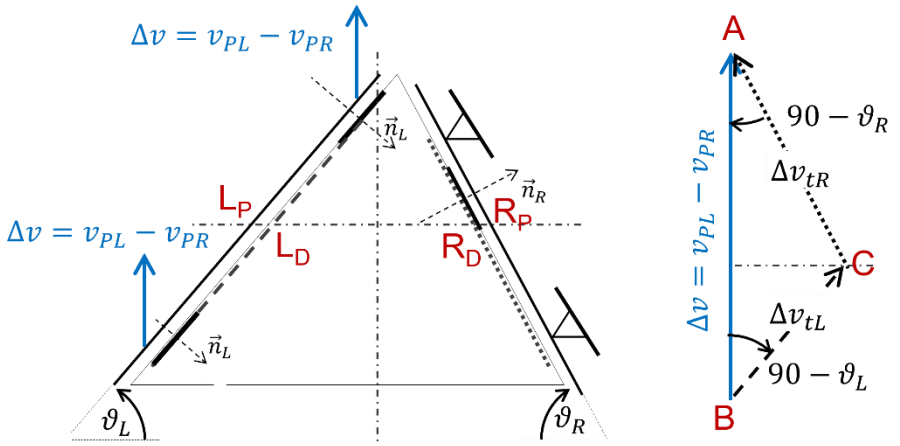

Fig. C.1: Relative sliding velocities in full sliding

Since the sliding damper-platform velocities depend on the relative motion between platforms, Fig. C.1 most conveniently represents the case where the right platform is fixed and the left platform of moves vertically by the amount $\Delta v = v_{PL} - v_{OR}$, Fig. 6. Segment AC represents the vector Δv_{tR} of sliding motion of the damper against the right platform, R_D against R_P. A point belonging to the left platform, on L_P moves together with a point R_D on the damper and in addition has a relative sliding motion Δv_{tL}, represented by segment BC, the sum being the absolute motion of left platform.

This trivial gives:

$$\Delta v_{tR} = \Delta v \frac{1}{\cos\vartheta_R\,(\tan\vartheta_R + \tan\vartheta_L\,)} \tag{C.1}$$

$$\Delta v_{tL} = \Delta v \frac{1}{\cos\vartheta_L\,(\tan\vartheta_R + \tan\vartheta_L\,)} \tag{C.2}$$

With:

F_{R1}^{+}: contact force in R_1 during the forward half cycle
F_{R1}^{-} : contact force in R_1 during the backward cycle
F_{L1}^{+}: contact force in L_1 during the forward half cycle
F_{L1}^{-} : contact force in L_1 during the backward cycle
F_{L2}^{+}: contact force in L_2 during the forward half cycle
F_{L2}^{-} : contact force in L_2 during the backward cycle

During sliding the respective tangential components are:

$$F_{Xy}^{+} \sin\varphi_X \tag{C.3}$$

Since all forces are proportional to the damper radial force F_D , the following factors f_{Xy}^{+} are defined so that:

$$F_{Xy}^{\pm} = f_{Xy}^{\pm}\, F_D \tag{C.4}$$

Work dissipated on a contact during the forward and the backward half-cycle are:

$$W_{R1} = F_D\, \Delta v_{tR}\, [\sin\varphi_R\ (f_{R1}^{+} + f_{R1}^{-})] \tag{C.5}$$

$$W_{L1} = F_D\, \Delta v_{tL}\, [\sin\varphi_L\ (f_{L1}^{+} + f_{L1}^{-})\,] \tag{C.6}$$

$$W_{L2} = F_D\, \Delta v_{tL}\, [\sin\varphi_L\ (f_{L2}^{+} + f_{L2}^{-})\,] \tag{C.7}$$

The dissipated energy can be calculated as well from the cycle of the moment M_P applied to the platform. It was demonstrated in [16] that aside the more standard method of directly using the contact force components on the platform, a more synthetic formula holds as well, that neglecting the angular pitch between blades, i.e, adopting the "parallel blade" model of Fig. 6:

$$M_p = \left(F_{L,v} - F_{R1,v}\right) \frac{q^*}{2} \tag{C.8}$$

where:

$F_{L,v} = F_D\, f_{L,v}$: total resultant contact force on the damper's left side
$F_{R1,v} = F_D\ f_{R1,v}$: contact force on the damper's right side, i.e., force on R_1
q^* : the distance between platforms, Fig. 6.

Then with:

M_P^{+} : moment in the forward half-cycle
M_P^{-} : moment in the backward half-cycle
the moment difference:

$$\Delta M_P = M_P^{+} - M_P^{-} = F_D \frac{q^*}{2}\left[\left(f_{L,v}^{+} - f_{R1,v}^{+}\right) - \left(f_{L,v}^{-} - f_{R1,v}^{-}\right)\right] \tag{C.9}$$

Note that thanks to (B.9) all the necessary information is contained in in the "equilibrium track" diagram, or "force" Base-Cycle. In fact, all factors $f_{\dots}^{\pm}$ involved in these equations are seen as in the example of Fig. C.2, cycle for μ =0.5 in the case 90L, Fig. 19.

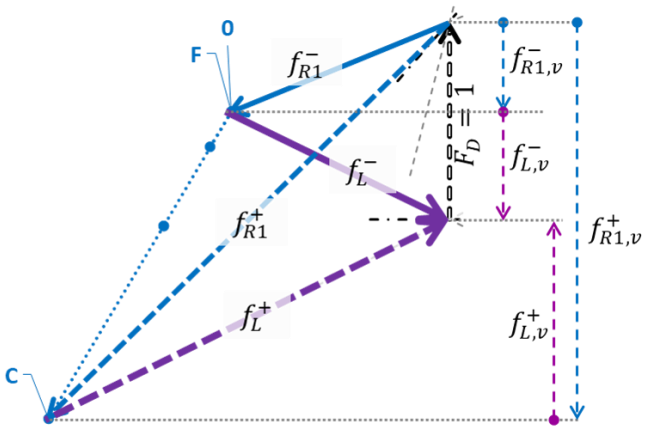

Fig. C.2: Left and right resultant forces on damper on "equilibrium track", cycle-start and half-cycle, case 90L, $\mu = 0.5$ of Fig. 19

For a rotation range $\Delta\psi_P$ such that, Fig. 15:

$$\Delta v = \Delta\psi_P \frac{q^*}{2} \tag{C.10}$$

Then, a sliding forward and backward motion of angular range $\Delta\psi_P$ produce on contacts, (C.1), (C.2) into (C.5), (C.6), (C.7) with (C.10):

$$W_{R1} = F_D \Delta v \left[\frac{\sin\varphi_R}{\sin\vartheta_R} \frac{\tan\vartheta_R}{(\tan\vartheta_R + \tan\vartheta_L)} (f_{R1}^+ + f_{R1}^-)\right] = F_D \Delta\psi_P \frac{q^*}{2} w_{R1} \tag{C.11}$$

$$W_{L1} = F_D \Delta v \left[\frac{\sin\varphi_L}{\sin\vartheta_L} \frac{\tan\vartheta_L}{(\tan\vartheta_R + \tan\vartheta_L)} (f_{L1}^+ + f_{L1}^-)\right] = F_D \Delta\psi_P \frac{q^*}{2} w_{L1} \tag{C.12}$$

$$W_{L2} = F_D \Delta v \left[\frac{\sin\varphi_L}{\sin\vartheta_L} \frac{\tan\vartheta_L}{(\tan\vartheta_R + \tan\vartheta_L)} (f_{L2}^+ + f_{L2}^-)\right] = F_D \Delta\psi_P \frac{q^*}{2} w_{L2} \tag{C.13}$$

and the work of the platform moment, from (B.9):

$$W_M = F_D \Delta\psi_P \frac{q^*}{2} \left[(f_{L,v}^+ - f_{R1,v}^+) - (f_{L,v}^- - f_{R1,v}^-)\right] = F_D \Delta\psi_P \frac{q^*}{2} w_M \tag{C.14}$$

The non-dimensional factors:

$$w_{R1},\ w_{L1},\ w_{L2},\ w_M$$

are here named "work shape factors". Fig. C.3 represents an example dissipated work of contact forces due to Base-Cycle, hatched area, and the part due to full sliding, parallelogram of area $\Delta M_P\ \Delta\psi_P$.

The value of w_M is proportional to the full-slip moment difference M_P, eq. (A9). The values calculated in row 4, 5 of Tables B1.2, B2.2, B3.2, B4.2, B5.2 are a final check of the correctness of the calculations, as it always found:

$$w_M = w_{R1} + w_{L1} + w_{L2} \tag{C.15}$$

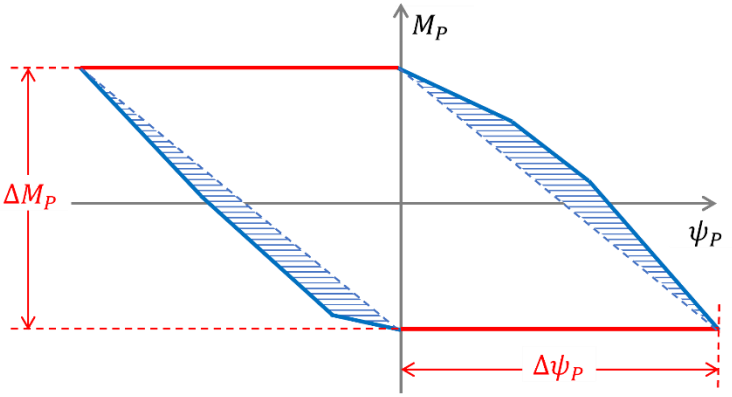

Fig. C.3: Dissipative frictional work, hatched from Base-Cycle, void parallelogram from full sliding